

# **CFD Analysis for Advanced Accumulator**

**Non-proprietary Version**

**August 2011**

**© 2011 Mitsubishi Heavy Industries, Ltd.  
All Rights Reserved**

## Revision History

Revision	Page	Description
0	All	Original issued
1	-	<b>Remarks</b> All of calculations are updated by using Fluent Ver.12.0, where rev.0 of this technical report was reported by based on the calculation due to ver.6.3. Additional calculations are added to evaluate numerical uncertainty. Some sensitivity analyses are added to justify calculation method The followings items are revised in accordance with the revision of the proprietary scopes;
	iii	The title of Appendix-A is changed. Appendix B to K are added.
	iv	Table C-1 is added.
	v, vi	The figure of Appendix-A and Appendix B to K is changed and added, respectively.
	vii to ix	Many symbols and acronyms are added.
	2-1	The objective to evaluate CFD-evaluated Scale Effect is added.
	3-2	To use BPG (Best Practice Guideline) is described. The condition of tank water level is changed and the way is described for large flow
	3-3	The condition of tank water level is changed and the way is described for small flow. The title and content of Sec. 3.2.1(3) are changed.
	3-6	Description of Y+ and GCI regarding mesh is added.
	3-7,8	Mesh configuration shown in Figure 3.2-3 and 3.2-4 are revised.
	3-9	Version of Fluent is changed from 6.3.26 to 12.0. Time dependence is changed from Steady-State to Unsteady-State Calculation for small flow. Description of multiphase model is separated from one of Cavitation model. Description of note regarding RSM model is updated. Description of note regarding near-wall treatment is updated.
	3-10	Description regarding Singhal model is added to note 8.
	3-11	Total number of calculation points is increased. Description of calculation condition to obtain the GCI is added.
	3-12	Test cased for GCI is added.
	3-13	New calculation points are added in Figure 3.3-1.
	3-14	It is added that details of boundary conditions for small flow is described Appendix-D.

## **Revision History (Cont.)**

Revision	Page	Description
1	3-14	Description of note 1 is revised
	3-15	Description of note 2 is revised
	3-17, 18	Description of flow structure is revised
	3-19	Sec. 3.5.1(3) is added.
	3-20	Calculation results regarding flow structure shown in Figure 3.5-1 is updated.
	3-21 to 24	Figures 3.5-2 to 3.5-5 are added.
	3-25	Calculation results regarding the relationship between flow rate coefficient and cavitation factor shown in Figure 3.5-6 is updated.
	3-26	Description of flow structure is revised.
	3-34 to 38	Bias error and uncertainty of scale effect is introduced as CFD-evaluated Scale Effect.
	4-1	Result of CFD-evaluated Scale Effect is added.
	5-1	References from 1) to 3) are revised. References from 4) to 16) are added.
	A-1 to end of K	The title of Appendix-A is changed. Appendix-B to -K are added.
2	x	Description of acronyms are revised.
	1-1	Section 1.1 is added.
	2-1	Descriptions are revised.
	3-1 to 3	Descriptions are revised.
	3-4	Table 3.2-1 is added.
	3-6, 7 3-9 to 14	Descriptions are revised.
	3-15	Figure 3.3-1 is revised.
	3-16 to 18	Descriptions are revised.
	3-19 to 21	Description of 3.5 is revised.
	3-23	Figure 3.5-2 is revised.
	3-26	Figure 3.5-5 is revised.
	3-27	Figure 3.5-6 is revised.
	3-28	Table 3.5-1(a) and 3.5-1(b) are added.
	3-29, 30	Description of 3.5.2 is revised.
	3-35	Figure 3.5-9 is revised.
	3-36	Figure 3.5-10(a) and 3.5-10(b) are revised.
	3-36 to 40, 3-42	Description of 3.5.3 is revised.
	4-1	Description of 4.0 is revised.
	5-1, 2	References 3) and 9) are revised. References from 17) to 19) are added.

## **Revision History (Cont.)**

Revision	Page	Description
2	A-1	Description of Appendix-A is revised.
	-	Figure B1-1 of MUAP-09025-P (R1) is deleted.
	B-1 to B-18	Appendix-B is revised.
	B-11	Figure B3-3 is revised.
	B-13	Table B3-5 and B3-6 are added.
	B-14	Description of B-3(3) is revised. Explanation of additional 3 GCI calculations are added.
	B-14	Table B3-7 is added.
	B-15, 16	Figure B3-5 and B3-6 are added.
	B-17	Table B3-8 is added.
	B-18	Description of B-4 is revised.
	-	Figure C-1 to C-3 of MUAP-09025-P (R1) is deleted.
	C-4 to 6	Description of Appendix-C is revised.
	C-8	Figure C-2 is added.
	C-9, 11, 12	Description of Appendix-C is revised.
	D-1	Table D-1 is revised.
	E-1	Description of Appendix-E is added.
	E-10	Figure E-5(b) is revised.
	F-1	Description of Appendix-F is added.
	F-12 to F-15	Figure F-6(a) to (d) are added
	F-16, 17	Figure F-7(a) and (b) are added
	H-1	Description of Appendix-H is revised.
	I-1 to 10	Appendix-I is revised add an evaluation of the impact of cavitation occurrence on flow coefficient..
	-	Appendix-J of MUAP-09025-P (R1) is deleted.

© 2011  
**MITSUBISHI HEAVY INDUSTRIES, LTD.**  
All Rights Reserved

This document has been prepared by Mitsubishi Heavy Industries, Ltd. ("MHI") in connection with the U.S. Nuclear Regulatory Commission's ("NRC") licensing review of MHI's US-APWR nuclear power plant design. No right to disclose, use or copy any of the information in this document, other than by the NRC and its contractors in support of the licensing review of the US-APWR, is authorized without the express written permission of MHI.

This document contains technology information and intellectual property relating to the US-APWR and it is delivered to the NRC on the express condition that it not be disclosed, copied or reproduced in whole or in part, or used for the benefit of anyone other than MHI without the express written permission of MHI, except as set forth in the previous paragraph.

This document is protected by the laws of Japan, U.S. copyright law, international treaties and conventions, and the applicable laws of any country where it is being used.

Mitsubishi Heavy Industries, Ltd.  
16-5, Konan 2-chome, Minato-ku  
Tokyo 108-8215 Japan

## **Abstract**

The Advanced Accumulator (ACC) developed by MHI functions to switch flow rates automatically from a large flow rate to small flow rate as a requirement for the Loss of Coolant Accident (LOCA) event. The function is achieved by the flow damper in the accumulator tank. For the purpose of understanding the flow characteristics and verifying the performance of the ACC, the “Full-Height 1/2 Scale Confirmation Test”, which uses the full height of the test tank and the standpipe, has been conducted (Ref.1). For flow with large Reynolds numbers, minimal influence from viscous effects is anticipated. Therefore, the 1/1 scale ACC prototype with even larger Reynolds numbers, will also have similar hydraulic performance as the 1/2 scale model. MHI proposes to apply the measured 1/2 scale hydraulic performance to the 1/1 scale ACC.

However, since there is little detailed information measured in the vortex chamber of the flow damper and near the throat section in existing experiments, there may not be enough evidence to validate extrapolation to the 1/1 scale. To provide an adequate explanation, sufficient understanding about the flow dynamics of ACC is important, especially flow inside the vortex chamber and the connecting piping (such as throat, diffuser and injection piping), which may include cavitation phenomena.

Regarding the background mentioned above, a Computational Fluid Dynamics (CFD) analysis was applied to better understand the flow structure and the cavitation phenomena in the ACC, and to investigate the validity of extrapolating from 1/2 to 1/1 scale flow dampers.

In this investigation, CFD analyses with cavitation modeling options were conducted by using a 1/2 scale model and a 1/1 scale analytical model to show the similarity between the flow structure and flow characteristic performance (i.e., the flow rate coefficient) for the 1/2 and 1/1 scale sizes.

Below is the summary and conclusions about this report regarding the CFD analysis.

- The CFD prediction is feasible for large and small characteristic evaluations. In the 1/2 scale model analysis, the correlation between the flow rate coefficient ( $C_v$ ) and the cavitation factor ( $\sigma_v$ ) reasonably matched the measured data.
- The validity of the current evaluation approach (Refs.1 and 2) for the ACC performance (i.e., the extrapolation from scale model experiment and the characteristic equations) is supported by the scale effect obtained from the CFD models. The CFD-Evaluated Scale Effect between the calculated data in the 1/2 scale model and the 1/1 scale model was shown to consist mainly of CFD uncertainty. The CFD-Evaluated Scale Effect can be accounted for in the evaluation of the 1/1 scale ACC hydraulic performance (Refs. 1 and 2).

## **Table of Contents**

List of Tables .....	iv
List of Figures .....	vi
List of Acronyms and Symbols .....	ix
1.0 INTRODUCTION .....	1-1
1.1 Report Outline.....	1-1
2.0 OBJECTIVE.....	2-1
2.1 Background .....	2-1
2.2 Objective .....	2-1
3.0 CFD ANALYSIS .....	3-1
3.1 System Descriptions .....	3-1
3.2 Analysis Models .....	3-2
3.3 Test Case for Analysis.....	3-13
3.4 Boundary Conditions.....	3-16
3.5 Analysis Results.....	3-19
4.0 CONCLUSIONS .....	4-1
5.0 REFERENCES .....	5-1
Appendix-A    Calculation of GCI.....	A-1
Appendix-B    Scale up Capability of Turbulence Model .....	B-1
Appendix-C    Selection of Cavitation Model .....	C-1
Appendix-D    Consideration for Boundary Condition in Small Flow Injection .....	D-1
Appendix-E    Flow structure for Large Flow .....	E-1
Appendix-F    Flow structure for Small Flow .....	F-1
Appendix-G    Y+ Profile .....	G-1
Appendix-H    Validity Evaluation of Tolerance Interval.....	H-1
Appendix-I    Effect of Cavitation on Small Flow Hydraulic Performance .....	I-1
Appendix-J    Details of Comparison Error for Large Flow .....	J-1

## **List of Tables**

Table 3.2-1	Comparison of Main Dimensions.....	3-4
Table 3.3-1	Test Cases and Time Points for Calculation .....	3-14
Table 3.3-2	Test Cases for GCI Calculation .....	3-14
Table 3.4-1	Boundary Condition Data for Calculation .....	3-18
Table 3.5-1(a)	Characteristic Equation and Calculation Results for Flow Rate Coefficient (Large Flow) .....	3-28
Table 3.5-1(b)	Characteristic Equation and Calculation Results for Flow Rate Coefficient (Small Flow) .....	3-28
Table 3.5-2	Factors for Calculating the Two-Sided 95% Probability Intervals for A Normal Distribution (Ref. 16)) .....	3-39
Table 3.5-3	Uncertainties in ACC Flow Model (Large Flow).....	3-41
Table 3.5-4	Uncertainties in ACC Flow Model (Small Flow).....	3-41
Table A-1	Calculation Procedure of GCI for 1/2 Scale Model CFD ( $\phi$ = Flow Rate Coefficient Cv) .....	A-6
Table A-2	Calculation Procedure of GCI for 1/1 Scale Model CFD ( $\phi$ = Flow Rate Coefficient Cv) .....	A-6
Table A-3	Calculation Procedure of GCI for 1/2 Scale Model CFD ( $\phi$ = Tank Inlet Pressure Pg) .....	A-7
Table A-4	Calculation Procedure of GCI for 1/1 Scale Model CFD..... ( $\phi$ = Tank Inlet Pressure Pg) .....	A-7
Table B2-1	Examples of Tuning the $\epsilon$ Equation .....	B-4
Table B3-1	Calculation Condition and Calculation Results Before and After Tuning for 1/2 Scale Model Calculation .....	B-9
Table B3-2	Effect of Tuning on Mean Cv Comparison Error (Small Flow) .....	B-10
Table B3-3	Comparison of Flow Structure by Tuning for Small Flow Injection .....	B-11
Table B3-4	Calculation Condition and Calculation Results Before and After Tuning for Scale Effect .....	B-12
Table B3-5	Calculation Conditions of Tuned CFD .....	B-13
Table B3-6	Calculation Results of Tuned CFD .....	B-13
Table B3-7	GCI Change Due to Tuning of Turbulence Model .....	B-14
Table B3-8	Calculation Procedure of GCI ( $\phi$ = Flow Rate Coefficient Cv).....	B-17
Table C-1	Capabilities and Limitations of Three Cavitation Models in FLUENT 12.0.....	C-3



---

Table C-2	Calculation Conditions for Singhal and ZGB Models.....	C-6
Table C-3	Scale Effects in Singhal and ZGB Models for Large Flow .....	C-6
Table D-1	Calculation Conditions of CFD .....	D-1
Table D-2	Calculation Results of CFD .....	D-1
Table H-1	Factors for Calculating the Two-Sided 90% and 95% Probability Intervals for a Normal Distribution (Ref.15)) .....	H-1
Table I-1	CFD Boundary Conditions for Sensitivity Analysis Regarding Cavitation Occurrence .....	I-2
Table I-2	Calculation Results (1/2 Scale) .....	I-9
Table I-3	Calculation Results (1/1 Scale) .....	I-9

---

## **List of Figures**

Figure 3.2-1	Analysis Models for 1/1 Scale .....	3-5
Figure 3.2-2	Analysis Models for 1/2 Scale .....	3-6
Figure 3.2-3	Mesh Configurations of Vortex Chamber for 1/2 and 1/1 Scale Model for Large Flow .....	3-9
Figure 3.2-4	Mesh Configurations of Vortex Chamber for 1/2 and 1/1 Scale Model for Small Flow .....	3-10
Figure 3.3-1	Calculation Points on Flow Characteristics of Flow Damper .....	3-15
Figure 3.5-1(a)	Flow Structure in Vortex Chamber (Large Flow).....	3-22
Figure 3.5-1(b)	Flow Structure in Vortex Chamber (Small Flow).....	3-22
Figure 3.5-2	General Flow Structure .....	3-23
Figure 3.5-3	Static Pressure Distribution (Small Flow, Fine Mesh, Case 3, 43 sec).....	3-24
Figure 3.5-4	Void Fraction Distribution (Small Flow, Fine Mesh, Case 3, 43 sec).....	3-25
Figure 3.5-5	Reverse Flow Confirmation.....	3-26
Figure 3.5-6(a)	Comparison between Test Results and Calculation Results for Flow Rate Coefficient in Large Flow Condition .....	3-27
Figure 3.5-6(b)	Comparison between Test Results and Calculation Results for Flow Rate Coefficient in Small Flow Condition .....	3-27
Figure 3.5-7(a)	Flow Structure in Vortex Chamber (Case 3 Large Flow 5 sec).....	3-31
Figure 3.5-7(b)	Flow Structure in Outlet Nozzle (Case 3 Large Flow 5 sec) .....	3-32
Figure 3.5-8(a)	Flow Structure in Vortex Chamber (Case 3 Small Flow 43 sec).....	3-33
Figure 3.5-8(b)	Flow Structure in Outlet Nozzle (Case 3 Small Flow 43 sec) .....	3-34
Figure 3.5-9	Comparison between 1/2 and 1/1 Scale of CFD Result .....	3-35
Figure 3.5-10(a)	Relationship between Flow Rate Coefficient and Scale (Large Flow).....	3-36
Figure 3.5-10(b)	Relationship between Flow Rate Coefficient and Scale (Small Flow) .....	3-36
Figure A-1	CFD Mesh Configurations (Fine Mesh) .....	A-4
Figure A-2	CFD Mesh Configurations (Normal Mesh) .....	A-4
Figure A-3	CFD Mesh Configurations (Coarse Mesh).....	A-5
Figure A-4	Representative Grid Convergence Trend Curve for Cv (Flow Rate Coefficient) and Pg (Tank Pressure) with 1/2 Scale Model .....	A-8

Figure A-5	Representative Grid Convergence Trend Curve for Cv (Flow Rate Coefficient) and Pg (Tank Pressure) with 1/1 Scale Model .....	A-9
Figure B2-1	Axial Velocity Distribution of the Swirling Flow in the Rotating Pipe around the Pipe Axis .....	B-5
Figure B3-1	Test Results and Calculation Results for Flow Rate Coefficient (Large Flow Condition).....	B-7
Figure B3-2	Test Results and Calculation Results for Flow Rate Coefficient (Small Flow Condition).....	B-7
Figure B3-3	Effect of Tuning to Cv- $\sigma_v$ Map (Small Flow Condition) .....	B-11
Figure B3-4	Scale Effect for Cv by Tuning .....	B-12
Figure B3-5	Grid Convergence Trend Curve for “Cv” for case3-43 sec .....	B-15
Figure B3-6	Grid Convergence Trend Curve for “Cv” for case6-82 sec .....	B-16
Figure C-1	Void Fraction Distribution at the Throat (Case 3 Large Flow 5 sec, Fine Mesh) .....	C-7
Figure C-2	Total Pressure Loss of Vortex Chamber, Reducer and Diffuser .....	C-8
Figure D-1	Comparison of Inlet Boundary Conditions for Small Flow Injection (a) Void Fraction, (b) Velocity Contour, (c) Static Pressure .....	D-2
Figure E-1(a)	Flow Structure in Vortex Chamber (Case 3 Large Flow 20 sec).....	E-2
Figure E-1(b)	Flow Structure in Flow Damper (Case 3 Large Flow 20 sec) .....	E-3
Figure E-2(a)	Flow Structure in Vortex Chamber (Case 3 Large Flow 34 sec).....	E-4
Figure E-2(b)	Flow Structure in Flow Damper (Case 3 Large Flow 34 sec) .....	E-5
Figure E-3(a)	Flow Structure in Vortex Chamber (Case 6 Large Flow 5 sec).....	E-6
Figure E-3(b)	Flow Structure in Flow Damper (Case 6 Large Flow 5 sec) .....	E-7
Figure E-4(a)	Flow Structure in Vortex Chamber (Case 6 Large Flow 11 sec).....	E-8
Figure E-4(b)	Flow Structure in Vortex Chamber (Case 6 Large Flow 11 sec).....	E-9
Figure E-5(a)	Flow Structure in Vortex Chamber (Case 6 Large Flow 20 sec).....	E-10
Figure E-5(b)	Flow Structure in Flow Damper (Case 6 Large Flow 20 sec) .....	E-11
Figure E-6(a)	Flow Structure in Vortex Chamber (Case 6 Large Flow 50 sec).....	E-12
Figure E-6(b)	Flow Structure in Flow Damper (Case 6 Large Flow 50 sec) .....	E-13
Figure F-1(a)	Flow Structure in Vortex Chamber (Case 3 Small Flow 100 sec).....	F-2
Figure F-1(b)	Flow Structure in Flow Damper (Case 3 Small Flow 100 sec).....	F-3
Figure F-2(a)	Flow Structure in Vortex Chamber (Case 3 Small Flow 125 sec).....	F-4
Figure F-2(b)	Flow Structure in Flow Damper (Case 3 Small Flow 125 sec).....	F-5
Figure F-3(a)	Flow Structure in Vortex Chamber (Case 6 Small Flow 82 sec).....	F-6

Figure F-3(b)	Flow Structure in Flow Damper (Case 6 Small Flow 82 sec).....	F-7
Figure F-4(a)	Flow Structure in Vortex Chamber (Case 6 Small Flow 200 sec).....	F-8
Figure F-4(b)	Flow Structure in Flow Damper (Case 6 Small Flow 200 sec).....	F-9
Figure F-5(a)	Flow Structure in Vortex Chamber (Case 6 Small Flow 290 sec).....	F-10
Figure F-5(b)	Flow Structure in Flow Damper (Case 6 Small Flow 290 sec).....	F-11
Figure F-6(a)	Reverse Flow Region (1/2 Scale, Case 3 Small Flow) .....	F-12
Figure F-6(b)	Reverse Flow Region (1/2 Scale, Case 6 Small Flow) .....	F-13
Figure F-6(c)	Reverse Flow Region (1/1 Scale, Case 3 Small Flow) .....	F-14
Figure F-6(d)	Reverse Flow Region (1/1 Scale, Case 6 Small Flow) .....	F-15
Figure F-7(a)	Location of Max. value of Deference between Absolute Pressure and Critical Pressure of Cavitation (1/2 scale, Small Flow) .....	F-16
Figure F-7(b)	Location of Max. value of Deference between Absolute Pressure and Critical Pressure of Cavitation (1/1 scale, Small Flow) .....	F-17
Figure G-1	Y+ Distribution of Large Flow.....	G-1
Figure G-2	Y+ Distribution of Small Flow .....	G-2
Figure G-3	Shear Stress Distribution of Small Flow.....	G-2
Figure I-1(a)	Flow Structure in Vortex Chamber (at mid-height) .....	I-4
Figure I-1(b)	Flow Structure in Vortex Chamber and Outlet Nozzle .....	I-5
Figure I-1(c)	Critical Pressure of Cavitation and Void Fraction in vortex Chamber and Outlet Nozzle .....	I-6
Figure I-2	Velocity Distributions and Cavitation Pressure Margin at Throat .....	I-7
Figure I-3	Relative Average Total Pressure of Forward Flow Area .....	I-8
Figure J-1	Overlapping between Test Results and Calculation Results for Flow Rate Coefficient (Large Flow Condition) .....	J-2

## **List of Acronyms and Symbols**

ACC	Advanced Accumulator
APWR	Advanced Pressurized-Water Reactor
CFD	Computational Fluid Dynamics
$C_{T,95}(n)$	Factors for tolerance interval to contain at Least 95% of the population
COL	Combined License
$C_v$	Flow rate coefficient, (-)
$C_{v_{1/1},i}$	Flow rate coefficient in case i obtained by CFD for 1/1 scale ACC
$C_{v_{1/2},i}$	Flow rate coefficient in case i obtained by CFD for 1/2 scale ACC
$e_a^{21}$	Approximate relative error, (-)
$e_{ext}^{21}$	Extrapolated relative error, (-)
ECCS	Emergency Core Cooling System
$e_m$	Manufacturing error as relative standard deviation
$f_v$	Vapor mass fraction, (-)
$f_g$	Non-condensable gas mass fraction, (-)
Fs	Factor of safety, (-)
$F_{cond\_SH}$	Vapor condensation coefficient in Singhal model, = 0.01 (m/s)
$F_{vap\_SH}$	Vapor generation coefficient in Singhal model, = 0.02 (m/s)
$F_{cond\_ZGB}$	Vapor condensation coefficient in Zwart-Gerber-Belamri model, = 0.01(-)
$F_{vap\_ZGB}$	Vapor generation coefficient in Zwart-Gerber-Belamri model, = 50 (-)
g	Gravitational acceleration, (m/s <sup>2</sup> )
GCI	Grid Convergence Index, (-)
$GCI_{fine}^{21}$	Fine-grid convergence index, (-)
h	Representative cell size, (m)
LOCA	Loss of Coolant Accident
MHI	Mitsubishi Heavy Industries, Ltd
M.V.	Mean value of differences between 1/2 and 1/1 scale CFD
$n_B$	Number of bubbles per unit volume, (1/m <sup>3</sup> )
N	Total number of cells used for the computation, (-)
p	Observed order of accuracy, (-)
P	Local far-field pressure, (Pa)
$P_B$	Vapor bubble surface pressure, (Pa)
$P_g$	Tank pressure, (Pa)
$P_{sat}$	Vapor saturation pressure, (Pa)

$P_V$	Critical pressure of cavitation, (Pa)	
$r$	Grid refinement factor, (-)	
$R$	Vapor mass source term, (kg/(m <sup>3</sup> .s))	
RANS	Reynolds-averaged Navier-Stokes	
$R_B$	Vapor bubble radius, (m)	
$R_{B\_ZGB}$	Vapor bubble radius in Zwart-Gerber-Belamri model, = 10 <sup>-6</sup> (m)	
$R_c$	Mass transfer sink term due to vapor bubble collapse during the cavitation process, (kg/(m <sup>3</sup> .s))	
$R_e$	Mass transfer source term due to vapor bubble growth during the cavitation process, (kg/(m <sup>3</sup> .s))	
RCS	Reactor Coolant System	
RSM	Reynolds Stress Model	
S.D	Standard deviation of differences between 1/2 and 1/1scale CFD	
$u_{scale}$	Standard uncertainty of the scale effect bias estimated from CFD results	
$u_{SD}$	Standard uncertainty due to deviation from bias	
$u_{mesh}$	Standard uncertainty due to spatial discretization approximation for CFD calculations	
US	United States of America	
$V_{rel}$	Relative velocity between vapor bubble and liquid, (m/s)	
$V_v$	Vapor velocity, (m/s)	
We	Weber number, (-)	

#### Greek Letters

$\alpha$	Vapor volume fraction, (-)	
$\alpha_{nuc}$	Vapor bubble nucleation site volume fraction in Zwart-Gerber-Belamri model, = 5×10 <sup>-4</sup> (-)	
$\Gamma$	Diffusion coefficient, (kg/(m.s))	
$\kappa$	Turbulent kinetic energy, (m <sup>2</sup> /s <sup>2</sup> )	
$\rho$	Mixture density, (kg/m <sup>3</sup> )	
$\rho_l$	Liquid density, (kg/m <sup>3</sup> )	
$\rho_v$	Vapor density, (kg/m <sup>3</sup> )	
$\Delta\rho$	Density difference between liquid and vapor, (kg/m <sup>3</sup> )	
$\Delta V_i$	Volume of cell used for the computation, (m <sup>3</sup> )	
$\delta C_{V\_CFD}$	Scaling effects (bias) estimated from CFD results	
$\sigma$	Surface tension, (N/m) or Standard deviation	
$\sigma_v$	Cavitation Factor	
$\phi$	Key variable important to the objective of the simulation study for GCI	

## 1.0 INTRODUCTION

This report describes the Computational Fluid Dynamics (CFD) analysis results for the Advanced Accumulator (ACC) performed by Mitsubishi Heavy Industries, Ltd. (MHI). The purpose of this document is to show that the same ACC flow phenomena would occur in the test facility and the 1/1 scale prototype in the plant. Review of this Technical Report should facilitate review of the US-APWR Design Certification process and any subsequent Combined License (COL) which references the US-APWR Design.

The ACC is an accumulator tank with a flow damper that is partially filled with borated water and is pressurized with nitrogen. It is attached to the primary system with a series of check valves and an isolation valve and is aligned during operation to allow flow into the primary coolant system if pressure in the primary system drops below the pressure of the accumulator. The ACC design combines the known advantages and extensive operating experience of a conventional accumulator used for Loss of Coolant Accident (LOCA) mitigation in pressurized water reactors with the inherent reliability of a passive fluidic device to achieve a desired injection flow profile of reactor coolant without the need of any moving parts. Incorporation of the ACC into the US-APWR design and LOCA mitigation strategy simplifies a critically important safety system by integrating an inherently reliable passive safety component into the conventional Emergency Core Cooling System (ECCS). This design improvement will allow the elimination of low head safety injection pumps, and increase the amount of time available for the installed backup emergency power system to actuate. It is expected that the use of ACCs rather than low head safety injection pumps in the US-APWR design will reduce the net maintenance and testing workload at nuclear facilities while maintaining a very high level of safety.

Topical Report "The Advanced Accumulator", MUAP-07001 Revision 4 (Ref.1)), has been submitted to describe the principles of operation of the ACC, the important design features, and the extensive analysis and confirmatory testing program conducted. This Technical Report describes CFD analysis results to support discussion of scalability in the Topical Report.

### 1.1 Report Outline

This section provides an overview of the content and conclusions of the major sections in this report. Sections 1.0 and 2.0 provide an introduction and background to the ACC and outline the main objectives for the present CFD study. Section 3.0 describes the CFD analysis in detail. Section 4.0 provides the final results and conclusions of the CFD study, and Section 5.0 lists supporting references. The appendices contain detailed results supporting calculations and sensitivity analyses.

Details of the CFD analysis are contained in Section 3.0, which includes the following subsections:

- Section 3.1 provides a brief description of ACC operation and its safety function in the US-APWR plant.
- Section 3.2 describes the CFD model configuration including the ACC geometry modeled, the mesh configuration, and the chosen physical models and settings for the CFD analysis.

- Section 3.3 lists the test conditions chosen from the scaled testing described in Reference 1 which were chosen for further CFD analysis
- Section 3.4 outlines the boundary conditions for the CFD analysis and describes how these boundary conditions were derived from measurements taken during the scaled testing (Ref. 1).
- Section 3.5 provides the results of the CFD analysis and consists of the following three subsections:
  - Section 3.5.1, with the support of the appendices discussed below, verifies that the results are appropriate for quantifying a scaling effect. The general flow structures and flow coefficient behavior are similar between scales and consistent with the test observations and theoretical expectations described in Reference 1. Comparison to the measured test data and additional sensitivity analyses show that the CFD model configuration is sufficient for quantifying the scaling effect.
  - Section 3.5.2 provides the CFD results with explanations and comparisons to the measured test data.
  - Section 3.5.3 describes the methodology for evaluating the scale effect from the CFD results, including estimating the numerical and statistical uncertainty to quantify a final CFD-Evaluated Scale Effect.

The appendices to this report provide additional supporting information for the ACC CFD analyses. The appendices listed below contain sensitivity analyses and/or alternate calculations to justify and validate the results of the CFD analyses in Section 3.0:

- Appendix-B discusses the physical model for turbulence utilized in the analyses to evaluate the impact of modeling error in the CFD results for small flow, compared to the observed test values. The appendix performs additional CFD analyses with a modified version of the turbulence model and concludes that the CFD-Evaluated Scale Effect calculated using the generalized turbulent model is bounding.
- Appendix-C discusses the physical model for cavitation utilized in the analyses and includes sensitivity analyses using alternate cavitation models. The appendix concludes that alternate cavitation models do not significantly impact the CFD flow coefficients.
- Appendix-D performs sensitivity analyses for the small flow boundary conditions, and concludes that the type of boundary conditions employed do not significantly impact the CFD flow coefficients.
- Appendix-I analyzes the impact of potential cavitation during small flow. The appendix performs modified and bounding outlet pressure analyses to induce cavitation during small flow and demonstrates that cavitation occurrence does not impede flow or significantly affect the ACC flow coefficient.

The following appendices provide additional detailed results for the CFD analyses described in Section 3.0:



- Appendix-A provides details for the methodology and results for calculating the GCI to quantify the numerical uncertainty from the CFD results.
- Appendix-E provides detailed plots of flow structure for all analyzed CFD cases and conditions for large flow.
- Appendix-F provides similar plots of flow structures for all analyzed CFD cases for small flow.
- Appendix-G provides details of the CFD mesh for ensuring sufficient refinement to adequately model velocity gradients at the model walls.
- Appendix-H provides details for ensuring that the dispersion error in the CFD-Evaluated Scale Effect is adequately represented by the CFD results.
- Appendix-J provides details for ensuring that the large flow CFD results are adequately within the expected range of the measured test results.

## 2.0 OBJECTIVE

### 2.1 Background

Currently, for the purpose of understanding flow characteristics and verifying the performance of the ACC, the “Full-Height 1/2 Scale Confirmation Test” has been conducted (Ref.1). In flow with large Reynolds numbers, little influence of viscous effects is anticipated. Therefore, the 1/1 scale ACC prototype with even larger Reynolds numbers, will also have similar hydraulic performance as the 1/2 scale model. MHI proposes to apply the measured 1/2 scale hydraulic performance to the 1/1 scale ACC.

However, since there is little detailed information measured in the vortex chamber of the flow damper and near the throat section in existing experiments, there may not be enough evidence to validate the extrapolation to a 1/1 scale. To provide an adequate explanation, a sufficient understanding about the flow dynamics of the subject is important, especially flow inside the vortex chamber and the connecting piping (such as throat, diffuser and injection piping), which may include cavitation phenomena.

### 2.2 Objective

With regards to the background mentioned above, a CFD analysis was done to better understand the flow structure and the cavitation phenomena in the ACC, and to better validate the extrapolation from the 1/2 to the 1/1 scale model.

In this investigation, the CFD analysis with cavitation model option is conducted, for the 1/2 and 1/1 scale model. The calculated data is evaluated as follows.

- To evaluate the flow behavior at quasi-steady-states for both small and large flow rate conditions.
- To evaluate the correlation between relevant parameters in the calculations of the 1/2 scale model and its corresponding measured data.
- To evaluate the significance of the CFD-evaluated Scale Effect by comparing the uncertainty in the CFD calculations with the difference in flow coefficient results from the 1/2 and 1/1 scale CFD (i.e., CFD-evaluated bias)
- To quantify the CFD-Evaluated Scale Effect, including the uncertainty in CFD calculations for application to the 1/1 scale ACC hydraulic performance.

### 3.0 CFD ANALYSIS

#### 3.1 System Descriptions

The accumulator system is one of the subsystems of the ECCS. There are four accumulators, one for each reactor coolant cold leg. The accumulators are vertically mounted cylindrical tanks located outside each steam generator/reactor coolant pump housing. The accumulators are passive devices. They are filled with boric acid water and pressurized with nitrogen. The accumulators discharge water into the reactor cold leg when the cold leg pressure falls below the accumulator pressure.

The advanced accumulators of the US-APWR have internal passive flow dampers that inject large flow to refill the reactor vessel at the first stage of injection, and then reduce the flow as the accumulator water level drops. When the water level is above the top of the standpipe, water enters the flow damper through inlets at both the top of the standpipe and at the small flow pipe on the side of the vortex chamber, and injects water at a large flow rate. When the water level drops below the top of the standpipe, the water enters the flow damper only through the small flow pipe, and injects water at a low flow rate.

The two series check valves in the injection line to the reactor cold leg are held closed by the pressure differential between the Reactor Coolant System (RCS) and the accumulator charge pressure (approximately 1,600 pounds per square inch differential (psid)). The water level in the accumulator, boron concentration, and nitrogen charge pressure can all be remotely adjusted during power operations. The accumulators are non-insulated and assume thermal equilibrium at the containment normal operating temperature (approximately 70 to 120°F).

The accumulators are pressurized with nitrogen gas by a flow control valve in a common nitrogen supply line. The failure of the flow control valve is accommodated by a safety valve set at 700 psig with a (nitrogen) flow capacity of 90,000 ft<sup>3</sup> per hour. Likewise, each accumulator is equipped with a safety valve set at 700 psig and (nitrogen) flow capacity of 90,000 ft<sup>3</sup> per hour, which provides a margin from the normal operating pressure (640 psig), yet precludes overcharging by the associated safety injection pump.

### 3.2 Analysis Models

Analyses were conducted using a general-purpose thermal-hydraulics simulation software package, FLUENT. Characteristics of the flow in this simulation are strong swirl flow in the small flow condition and nozzle flow with cavitation in the large flow condition. FLUENT Ver.12 code was used, which includes a two-phase model and cavitation model (Ref.9)) to evaluate cavitation and can also analyze strong swirl flow.

Two separate analysis models were employed for the two different flow injection modes, i.e. large flow injection and small flow injection, in order to increase computational efficiency. It would be possible to calculate the two different flow injections with the same model. However, the flow phenomena and regions of interest differ between the two flow conditions (i.e., cavitation at nozzle throat for large flow injection and swirling flow in the vortex chamber for small flow injection). Therefore, use of the same model would result in unnecessary regions and increased calculation time and costs. The development of two different models suitable for large and small flow injections is intended to reduce the overall number of mesh elements and calculation load by focusing on the areas of interest for each flow condition.

These CFD analysis models were developed based on the “NEA/SCNI/R(2007)5 Best Practice Guidelines for the Use of CFD in Nuclear Reactor Safety Applications” (Ref.5)), the “Journal of Fluid Engineering Editorial Policy Statement on the Control of Numerical Accuracy” (Ref.7)) and the “Procedure for Estimation and Reporting of Uncertainty Due to Discretization in CFD Applications” (Ref.6)). These guidance documents recommend verification of the following analysis modeling items, which are discussed in the following sections:

- “Proper Geometrical Modeling” (Sec. 3.2.1 and Appendix-G)
- “Discretization and its uncertainty error estimation” (Sec. 3.2.2 and Appendix-A)
- “Selection of Appropriate Physics Modeling for the purpose”  
(Sec. 3.2.3, Appendices B and C)

### 3.2.1 Geometrical Modeling

Figures 3.2-1 and 3.2-2 show analysis models for each flow injection case.

#### (1) For Large Flow Injection

1. The model for large flow injection consists of the ACC tank, the height of which extends to the water level, the standpipe with the anti-vortex cap, the small flow pipe with the anti-vortex plate, the vortex chamber, the outlet nozzle and the injection pipe up to the point of pressure measurement during testing. (See note1)
2. The inner configuration of the flow damper is precisely modeled.
3. The casing thicknesses of the vortex chamber, ducting etc. are neglected.
4. The tank water level is changed for each analysis condition because the tank water level changes as a function of time throughout the injection.

(note1) Water level is set at stationary for steady state analysis.

#### (2) For Small Flow Injection

1. The model for small flow injection mainly consists of the ACC tank, the height of which is extended to the water level, the lower part of the standpipe (up to the water level), the small flow pipe with the anti-vortex plate, the vortex chamber, the outlet nozzle and the injection pipe up to the point of pressure measurement during testing. (See note2)
2. The inner configuration of the flow damper is precisely modeled.
3. The casing thicknesses of the vortex chamber, ducting etc. are neglected.
4. The water levels in the tank and the standpipe are changed for each analysis condition because the water levels change as a function of time throughout the injection.

(note2) The boundary conditions give flow-rate at the inlet of the small flow pipe and standpipe, and pressure at the exit of the injection pipe.

#### (3) Modeling of 1/2 and 1/1 Scale Model

1. CFD-evaluated Scaling Effects is estimated by comparing the predicted results in flow rate coefficients of 1/2 and 1/1 scale models, and including numerical uncertainty of the CFD calculations.
2. The dimensions of the 1/1 model were precisely doubled from those of the 1/2 scale model, except the standpipe height as shown in Table 3.2-1.
3. For both the 1/2 and 1/1 CFD models, the water levels in the tank and the standpipe are set at the same level for each analysis case as shown in Table 3.2-1. This is because the testing was performed for a 1/2 scale full-height model in which the heights of the test tank and water level were not scaled (see Ref. 1).

**Table 3.2-1 Comparison of Main Dimensions**

--	--	--



**(a) Analysis Model for Large Flow**



**(b) Analysis Model for Small Flow**

**Figure 3.2-1 Analysis Models for 1/1 Scale**



(a) Analysis Model for Large Flow



(b) Analysis Model for Small Flow

**Figure 3.2-2 Analysis Models for 1/2 Scale**



### 3.2.2 Mesh Configuration

Figure 3.2-3 and 3.2-4 show mesh configurations in the vortex chamber and the outlet nozzle. The number of mesh elements for each model is also shown in Figure 3.2-3 and 3.2-4.

For small flow injection, the velocity of vortex flow in the vortex chamber must be larger than that for the large flow injection. So a finer mesh configuration is employed in the regions near the chamber wall for small flow to properly resolve the boundary layer. For large flow, the critical wall regions are the areas in the outlet pipe downstream of the throat where cavitation may occur.

As for scaling, the mesh configuration is as follows.

Step1) The mesh configuration of the 1/2 scale model is set as baseline.

Step2) [ ]

Step3) [ ]

To make the  $Y^+$  value less than 300, the mesh thicknesses at the near-wall region are set as follows:

- (1) For the large flow condition, the mesh thickness is set so that  $Y^+$  becomes approximately 300 on the wall at the throat where the maximum velocity occurs (See Appendix-G).
- (2) For the small flow condition, the mesh thickness is set so that  $Y^+$  becomes approximately 70 on the inside walls of the vortex chamber (See Appendix-G).

Additionally, the meshes around the center of the vortex chamber are set to be especially [ ]

To estimate the numerical uncertainty due to discretization and evaluate the most probable calculation results, the "Grid Convergence Index (GCI)" is introduced in accordance with the NEA/SCNI/R(2007)5 standard (Ref.5)). The GCI procedure is performed as directed by the "Procedure for Estimation and Reporting of Uncertainty Due to Discretization in CFD Applications" (Ref.6)). Three different levels of mesh coarseness (i.e., coarse, normal, fine) are developed to estimate the uncertainty of the analysis result due to discretization error by following the GCI calculation method.

By the application of GCI, the following items have been achieved.

- Development of an analysis model with sufficiently fine mesh, which can properly evaluate the targeted phenomena.

- Estimation of the numerical uncertainty in the model resulting from discretization error.

The finest mesh models are used for the calculation of the CFD-Evaluated Scale Effects, which are shown in Figure 3.2-3, 3.2-4. The other mesh models and the procedure for calculating GCI are shown in Appendix-A.

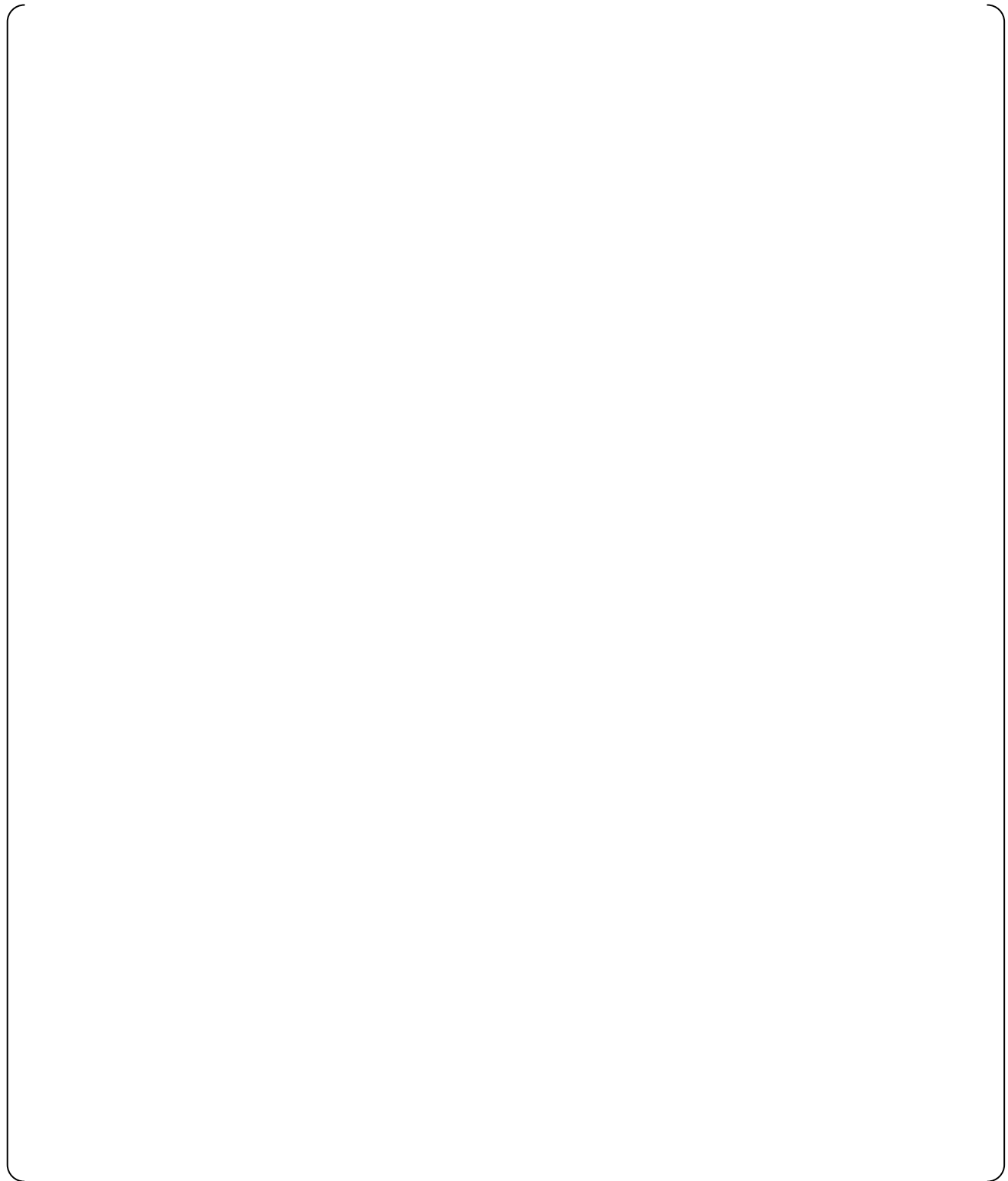


**Figure 3.2-3 Mesh Configurations of Vortex Chamber for 1/2 and 1/1 Scale Model for Large Flow**

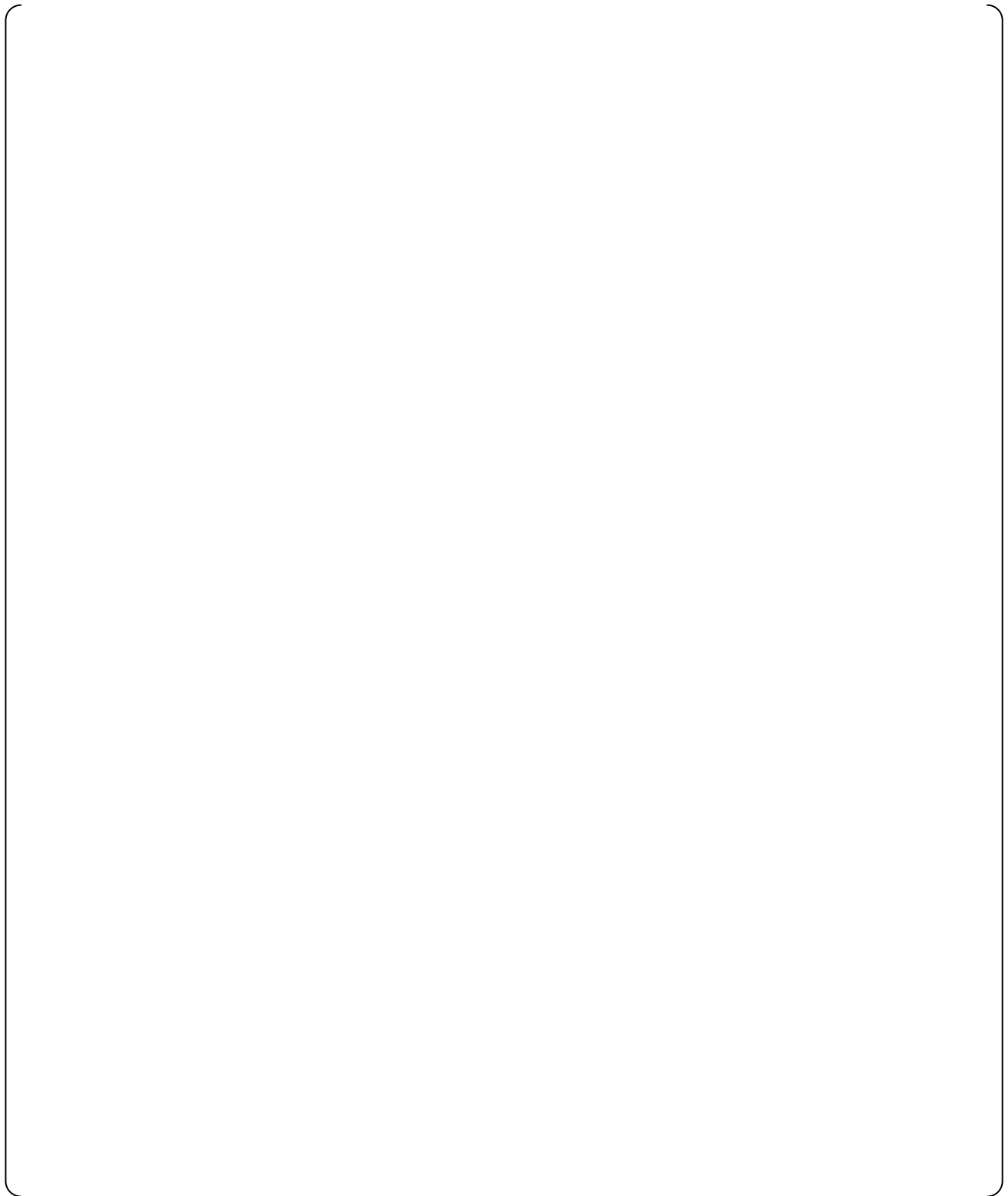


**Figure 3.2-4 Mesh Configurations of Vortex Chamber for 1/2 and 1/1 Scale Model for Small Flow**

### 3.2.3 Specification of the CFD Analysis

The CFD analysis was conducted and summarized on the following specification.

- **CFD Software:** FLUENT Ver. 12.0 (See 3.2.3(1))  
(A commercial CFD package developed by ANSYS, Inc.)
- **Time Dependence:** Steady-State Calculation for large flow  
Unsteady-State Calculation for small flow (See 3.2.3(2))
- **Type of Fluid:** Incompressible Viscous Fluid
- **Turbulence Model:** RSM (See 3.2.3(3))
- **Near-Wall Treatment:** [ ] (See 3.2.3(4))
- **Multiphase Model:** [ ] (See 3.2.3(5))
- **Cavitation Model:** [ ] (See 3.2.3(8))
- **Spatial Discretization:**
  - a) Momentum Equation: [ ] (See 3.2.3(6))
  - b) Pressure Term: [ ] (See 3.2.3(7))
  - c) Turbulence Source Terms: [ ] (See 3.2.3(6))
- **Gravity:** Gravity is considered and Operating Density is zero to evaluate occurrence of cavitation and ensure that body forces and density are evaluated separately for the fluid and vapor phases.
- **Other:** No Modeling for evolution of Dissolved Nitrogen Gas

Details of the selection of specification are described as follows.

#### (1) CFD Software

FLUENT Ver. 12.0 which includes three cavitation models is used instead of Ver.6.3 reported in rev.0 of this technical report so that cavitation models can be compared.

#### (2) Time Dependence

[ ]

#### (3) Turbulence Model

The Reynolds Stress Model (RSM) is a turbulence model which has greater potential to give accurate predictions for complex flows where swirl, rotation, and rapid directional

changes are dominating, compared with other models such as one-equation and two-equation models. The RSM solves transport equations for the Reynolds stresses and the dissipation rate, abandoning the isotropic eddy-viscosity hypothesis (Ref. 3)). [

]

#### **(4) Near-Wall Treatment**

[

]

#### **(5) Multiphase Model**

[

]

#### **(6) Spatial Discretization of Momentum Equation and Turbulence Source Terms**

[

]

#### **(7) Spatial Discretization of Pressure Term**

[

]

## (8) Cavitation Model

[

]

### 3.3 Test Case for Analysis

Among seven test cases using 1/2 scale test tank, Test Case3 and 6 were selected for CFD analysis conditions to cover cavitation factor in wide range (Ref.1)).

Test case 3 is the case in which the test tank has the highest initial pressure among all the test cases in order to acquire the data for high pressure designing, covering the range of small cavitation factors. The exhaust tank pressure was [ ] psig ([ ] MPa (gauge)) to simulate containment inner pressure following the blowdown phase during a large LOCA.

Test case 6 has the small pressure difference between test tank and exhaust tank in order to collect the data at large cavitation factor, covering the range of large cavitation factors.

Three or four time points are selected for each test case in order to cover the initial stage, middle stage(s), and the end stage.

Consequently, a total of 26 calculation points are analyzed for 1/2 scale and 1/1 scale. Test conditions and analysis time periods for Test Case 3 and 6 are shown in Table 3.3-1. Figure 3.3-1 shows these calculation points plotted on the 1/2 test result.

The test cases shown in Table 3.3-2 were used as the typical condition in the GCI evaluation described in Section 3.5.3. The earliest time point and the latest time point for each flow condition were used from each test case.





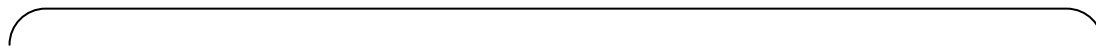


**Figure 3.3-1 Calculation Points on Flow Characteristics of Flow Damper**



### 3.4 Boundary Conditions

Table 3.4-1 shows the boundary conditions for this CFD investigation.

Basically, the measured data obtained from the 1/2 scale test were applied to the analysis models, i.e. tank pressure, tank outlet pressure, tank water level, standpipe water level. Total flow rate was calculated from the time series variation of tank water-level. Only some corrections and modifications are considered as needed for each model. For a physical reason, pressure boundaries were corrected to adjust pressure difference between 1/2 and 1/1 scale model (See note1 and note2). In the small flow injection case, for reasons of numerical calculation, the flow rate was used for the inlet boundary condition instead of the pressure boundary. This is because of the mass balance instability in the pressure boundary condition cases (See note2). In contrast, flow rate boundary cases gave stable results. These adjustments on boundary conditions contribute towards obtaining reasonable results for the evaluation of scale effects. (See Appendix-D)

#### For Large Flow Injection Case:

- Inlet Boundary Condition: Tank Pressure (See note1)
- Outlet Boundary Condition: Outlet Pressure (See note2)

#### For Small Flow Injection Case:

- Inlet Boundary Condition:
  - > Standpipe: Inlet Flow Rate (obtained by the time series variation of standpipe water-level. See Appendix-D)
  - > Small Flow Pipe: Inlet Flow Rate (See Appendix-D)
- Outlet Boundary Condition: Outlet Pressure (See note2)

#### **(note1)**

The analysis models consider the time series variation of tank water-level and the gravitational effect.

For the large flow 1/2 scale model analysis, pressure boundaries are applied at the inlet and outlet boundaries, and are set to the same pressure as the measured results. For the large flow 1/1 scale model analysis, the injection pipe elevation is 2 times higher than that of the 1/2 scale model due to scaling of the chamber outlet piping length, but the tank water-level is at the same elevation as that of 1/2 scale model. Therefore, the difference between the tank water-level and the height at the exit of the injection pipe of 1/1 scale model is smaller than that of 1/2 scale model, which affects the gravitational head.

To account for this effect, inlet pressure is corrected as follows to provide the same driving force conditions while maintaining the same cavitation factor (See Eq. (5-4) in Ref.1)):

$$P_{in1/1} = P_{in1/2} + \rho g (H_{out1/1} - H_{out1/2})$$

Where,

- $P_{in1/1}$  : Inlet pressure of 1/1 scale model  
 $P_{in1/2}$  : Inlet pressure of 1/2 scale model (Measured pressure)  
 $H_{out1/1}$  : The height at the exit of injection pipe of 1/1 scale model  
 $H_{out1/2}$  : The height at the exit of injection pipe of 1/2 scale model  
 $\rho$  : Density of water  
 $g$  : Acceleration of gravity

**(note2)**

The measured data obtained from 1/2 scale test were applied for the pressure condition at the exit of injection pipe.

Reference Pressure and Temperature for Fluid Properties Calculation (Such as viscosity, density, and saturated pressure etc.)

- Temperature : The measured data shown in Table 3.4-1 (Constant value)
- Pressure : Sum of the following pressure values
  - 1) Corrected pressure (Gauge pressure)
  - 2) Atmospheric pressure (Reference pressure)

**Table 3.4-1 Boundary Condition Data for Calculation**

### 3.5 Analysis Results

First, the applicability of the CFD model to the ACC is evaluated. Then the CFD model is used to evaluate the scale effect between the 1/2 and 1/1 scale model.

#### 3.5.1 Applicability of CFD to ACC

The applicability of CFD to the ACC is assessed by comparison of the results of the 1/2 scale test to the results of its CFD analysis such as flow structure and  $C_v$  value. The appendices to this report include additional results and sensitivity analyses for critical model parameters to further justify and validate CFD applicability, as discussed in the sections below.

##### (1) Flow Structure of 1/2 Scale Model

Flow structures of stream lines and flow vectors obtained by CFD are compared with the 1/5 scale visualized test which shows expected conceptual flow structures and has similar tendency to the 1/2 scale for the vortex chamber and the governing flow phenomena discussed in Reference 1. The CFD flow structure results are shown in Figure 3.5-1 and 3.5-3, and additional results are given in Appendices E and F. The chosen CFD case is comparatively similar to the test case shown in the figure. Additional details of the CFD flow structure are discussed below.

Figure 3.5-2 illustrates the flow in the vortex chamber on a simplified conceptual basis. As shown in Figure 3.5-2 a), in the large flow condition, the CFD results show that the flow from the standpipe and small flow pipe join together and the conflux flows out to the outlet nozzle without a strong vortex, which is similar to the flow structure of the test. Therefore, the main flow flows to the nozzle forming a U-shaped flow from the standpipe to the nozzle. This induces some flow separation at the inlet of the nozzle from the vortex chamber, but the separation does not continue to the throat due to the throttling effect of the reducer as shown in Figure E-1(b)-6(b) in Appendix-E. The pressure loss in this region is not significant because the throttling effect prevents significant flow separation. There are two permanent vortices in the vortex chamber as the flow reaches the far side of the chamber and returns to the nozzle outlet, shown in Figure 3.5-1. However, these vortices act as “rollers” to guide the main flow to the nozzle and do not develop large pressure losses. These permanent vortices differ from the strong vortex during the small flow phase described below. The flow velocity is accelerated from the outlet port of the vortex chamber to the throat in the reducer, due to the reduction of the flow area, and reaches a maximum at the throat. The static pressure decreases due to high velocity at the near-wall of the diffuser downstream of the throat, and this may cause cavitation. Thus, the majority of the pressure loss occurs at the diffuser downstream of the throat.

As shown in Figure 3.5-2 b), in the small flow condition, the CFD results show that the flow from the small flow pipe flows out to the outlet nozzle through a strong vortex in the vortex chamber, which is also similar to the flow structure of the tests. In this vortex, a forced vortex with the same diameter as the throat is formed, and a large pressure loss is developed in this region due to the viscosity. However, as shown in Figure 3.5-3 and the additional results in Appendix-E, the pressure distribution at the center of the vortex shows

that the static pressure is still much higher than the vapor pressure, and that cavitation does not occur. This can be observed in the void fraction distribution shown in Figure 3.5-4. In addition, centrifugal force increases pressure at the outer diameter of the vortex chamber and decreases pressure at the center of the vortex chamber. Viscosity reduces flow circulation in the boundary layers at the top and bottom faces of the chamber. These effects do not prevent radial flow at the boundary layers. Pressure recovers in the diffuser as the flow expands and allows reverse flow along the axis of the diffuser. This reverse flow exists in the vortex chamber, the outlet nozzle and the injection pipe. However as shown in Figure 3.5-5, the starting point of the reverse flow is approximately [ ] downstream from the outlet of the bend and back-flow does not initiate at the exit boundary.

Therefore, since it is confirmed that the 1/2 scale ACC CFD analysis shows similar flow structure to the expected conceptual flow and visualized data of 1/5 scale test, the CFD model can be applied to evaluate the scale effect.

## **(2) Relationship between Flow Rate Coefficient and Cavitation Factor**

The relationship between the flow rate coefficient ( $C_v$ ) and the cavitation factor ( $\sigma_v$ ) of the CFD model and test result is shown in Figure 3.5-6. The figure also shows the characteristic flow equations obtained from the test results with its corresponding 95% (2 standard deviation) uncertainty range, based on the instrument uncertainty and dispersion deviation (Ref.2). The uncertainty range is shown by the broken line in Figure 3.5-6.

The general trend of the flow rate coefficient vs. cavitation factor is consistent between the test and CFD results. For the large flow condition, the flow rate coefficient decreases as the cavitation factor decreases. For the small flow condition, the flow rate coefficient is almost constant over the range of cavitation factors. (Note that the very fine flow coefficient scale in Figure 3.5-6(b) magnifies the appearance of the minor differences in flow coefficient.)

As shown in Figures 3.5-6(a) and (b), Tables 3.5-1(a) and (b), for the large flow condition, the flow rate coefficients from the CFD results are within the range of instrument uncertainty and dispersion deviation of the test data, except for Case 3-5 sec. For the small flow condition, the flow rate coefficients from the CFD results are within the range of instrument uncertainty and dispersion deviation of the test data, except for Cases 3-125 sec and 6-82 sec. However, as shown in Tables 3.5-1(a)1 and (b)2, these points are very close to the lower  $2\sigma$  uncertainty limit of the characteristic equation, and these results are not significant outliers. Therefore, the CFD results adequately model the general behavior and overall tendency of the characteristic equation.

In summary, the CFD model is acceptable to evaluate the scale effect between the ACC 1/2 and 1/1 scale models using the flow structure and  $C_v$  value of the 1/2 scale model.

### (3) CFD Validation

As described above, the occurrence of cavitation for the large flow and fluid pattern such as vortex formation for small flow in this simulation can be predicted by the CFD model. In addition, the relation of the flow rate coefficient to the cavitation coefficient can also be predicted by the CFD. The CFD result is generally consistent with the model test result, although some differences can be observed. The CFD model solves the governing equations numerically and can evaluate the scale effects in principle. In addition, the physical models are developed from various experimental data and direct simulation data, and can also evaluate the scale effects. Detailed discussion with additional calculations to show the applicability of the adopted turbulence model, cavitation model, and boundary conditions are provided in the appendices described below.

Appendix-B discusses the development and scaling capability of the turbulence model. The turbulence model was developed empirically as a best-fit model for many flow applications and not specifically for the ACC flow application. However, the CFD-Evaluated scale effect is a differential evaluation between scales, and not an absolute evaluation between CFD and test data. Appendix-B address the difference between the CFD result and the scaled model test results for small flow. These appendices demonstrate that the turbulence model can be applied to the ACC phenomena by adjusting the empirical constants to reduce the (absolute) error due to the turbulence model generalizations with minimal effect on the calculated (differential) scale effects.

Appendix-C includes a discussion and sensitivity analysis of the available cavitation models. This appendix demonstrates that the chosen cavitation model is appropriate for use in the ACC CFD models and selection of cavitation model has a minimal impact on the CFD analyses.

Appendix-D demonstrates that the chosen boundary conditions for small flow also have minimal impact on the CFD results. Appendix-I evaluates the impact of the turbulence model generalizations and chosen boundary conditions to demonstrate that cavitation occurrence during small flow has a minimal impact on the hydraulic performance of the flow damper.

Appendix-J validates the large flow CFD results by demonstrating that the results are within the instrument uncertainty of the measured test results.

Therefore, the scale effects evaluated in this report using the generalized turbulence model, chosen cavitation model, and specified boundary conditions remain valid.



**Figure 3.5-1(a) Flow Structure in Vortex Chamber (Large Flow)**

**Figure 3.5-1(b) Flow Structure in Vortex Chamber (Small Flow)**





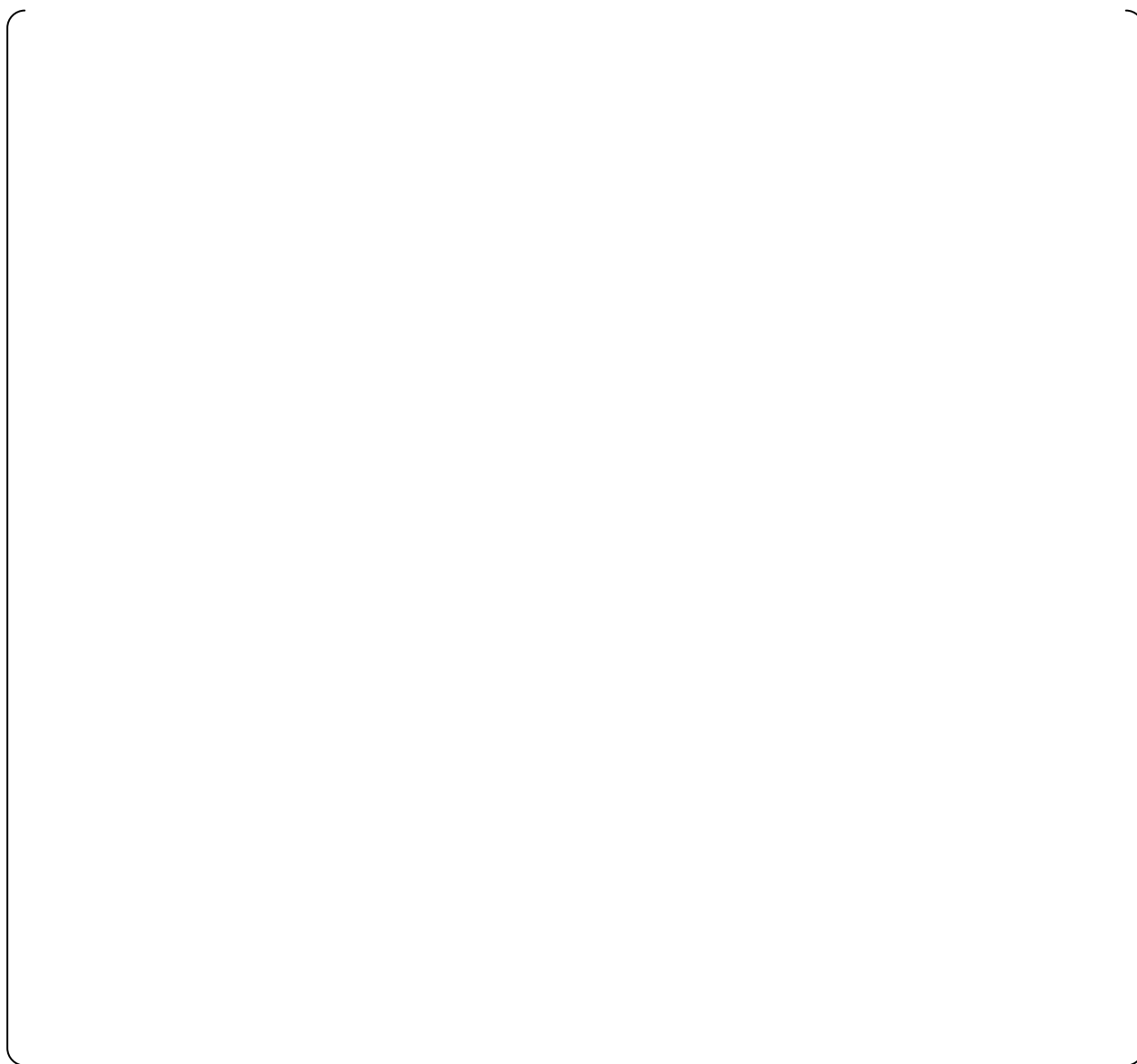


**Figure 3.5-2 General Flow Structure**



**Figure 3.5-3 Static Pressure distribution (Small Flow Fine Mesh, Case 3, 43 sec)**

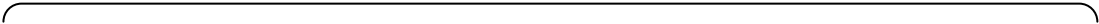
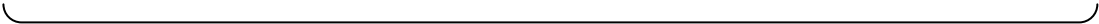
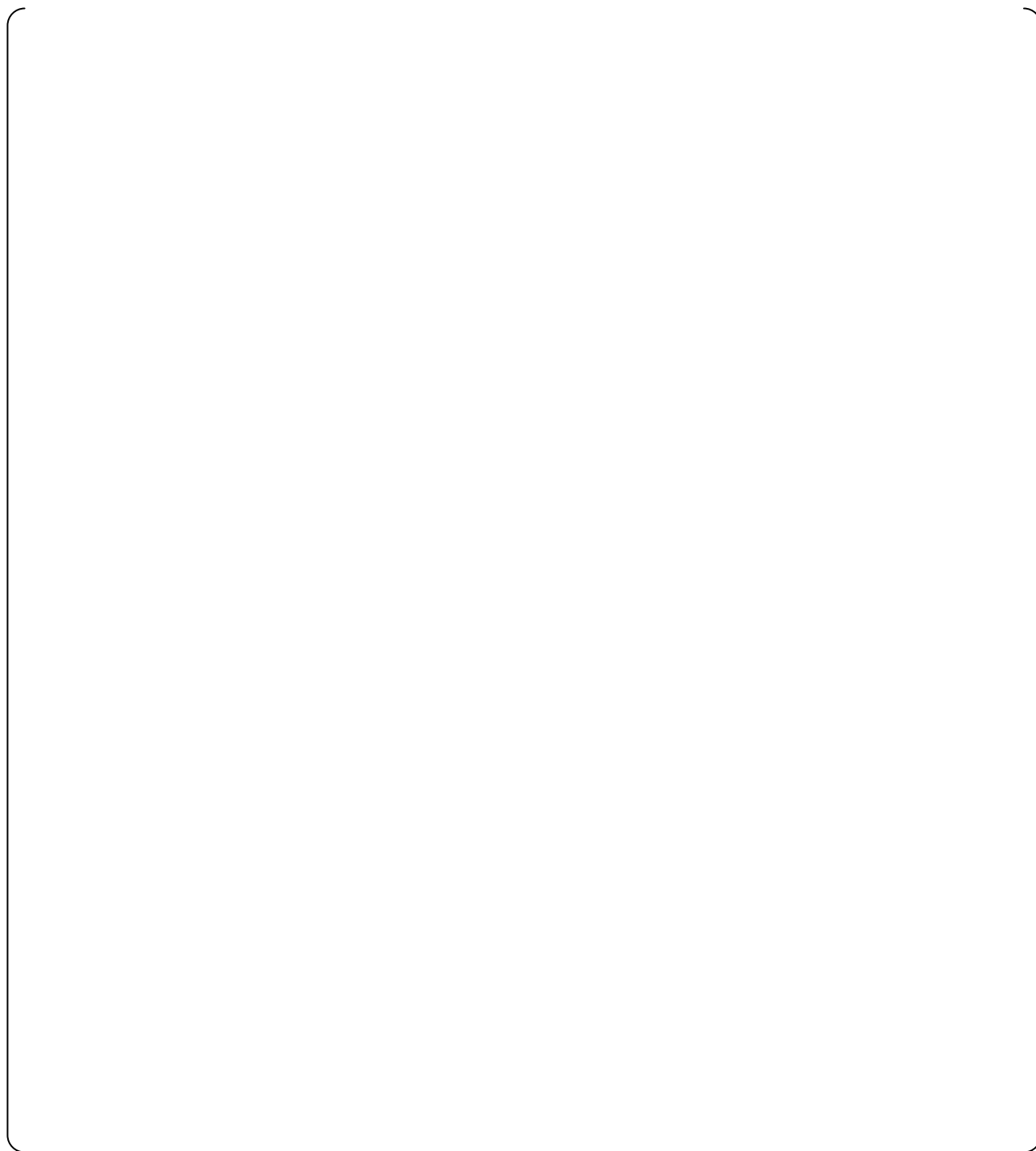


Figure 3.5-4 Void fraction distribution (Small Flow Fine Mesh, Case 3, 43 sec)





**Figure 3.5-5 Reverse Flow Confirmation**

**Figure 3.5-6(a) Comparison between Test Results and Calculation Results for Flow Rate Coefficient in Large Flow Condition**

**Figure 3.5-6(b) Comparison between Test Results and Calculation Results for Flow Rate Coefficient in Small Flow Condition**



### 3.5.2 Evaluation of Scale Effect Due to CFD

The scale effect is evaluated by comparing the CFD results such as flow structure and  $C_v$  value between the 1/2 and 1/1 scale models.

#### (1) Comparison of flow structure

The flow structure results comparing the 1/2 and 1/1 scale CFD models are shown in Figure 3.5-7 (Large Flow Case 3-5 sec) and Figure 3.5-8 (Small Flow Case 3-43 sec). The flow structures of the other cases are summarized in Appendices E and F.

The flow structure CFD results in both large and small flow conditions for the 1/1 scale model are similar to that of the 1/2 scale model in regards to static pressure, flow vector and void fraction as follows. The effect of these differences on hydraulic performance (i.e., flow coefficient) is quantified through the CFD-Evaluated Scale Effect calculated in Section 3.5.3.

#### Large Flow Injection

CFD results of both scale models show that the void fraction becomes large as the cavitation factor becomes small (See Figure 3.5-7 and Appendix-E). The flow behavior from the CFD model results for the large flow condition show a similar tendency between the 1/2 and 1/1 scale model regarding void generation.

CFD results also show that the two flows from the stand pipe and small flow pipe flow together in the vortex chamber without forming a strong vortex within the vortex chamber (See Fig 3.5-7(a)). This conflux separates into a portion that directly exits the outlet nozzle and a portion that exits the nozzle after reaching the far wall of the chamber and forming a small recirculation vortex in the vortex chamber. This recirculation vortex differs from the strong vortex which causes the large pressure drop during small flow. Some differences in the flow structures within the vortex chamber are observed between scales in confluence and separation. These will cause differences in the velocity profiles at the exit of the vortex chamber, which in turn will cause differences in the velocity, pressure and void distribution at the outlet nozzle as shown in Fig 3.5-7(b).

Since the flow resistance for large flow is dominated by the throat of the outlet nozzle, differences in flow structure within the vortex chamber would have limited effect on the overall flow resistance. However, the quantitative CFD results shown in Section 3.5.3(2) demonstrate that the effect is very small. In other words, the overall flow resistance for large flow is insensitive to the differences in flow structure within the vortex chamber between scales. This discussion also applies to the results shown in Appendix-E

#### Small Flow Injection

A strong vortex in the vortex chamber is confirmed for both the 1/2 and 1/1 scale models as shown in Fig. 3.5-8. In addition, both scale models do not show void generation at the center of the vortex or the outlet nozzle. (See Appendix-I for additional discussion of cavitation occurrence during small flow.) Similar reverse flows from the outlet nozzle to

the vortex chamber and velocity distributions are observed between the 1/2 and 1/1 scale models (See Fig. 3.5-8). However, there are slight differences in static pressure in the vortex chambers and the outlet nozzles. The effect of these differences on the flow rate coefficient is evaluated in Section 3.5.3(2). This discussion also applies to the results shown in Appendix-F.

## **(2) Comparison of relationship between flow rate coefficient and cavitation factor**

In both large and small flow conditions, the flow rate coefficients agree well between 1/1 scale model and 1/2 scale model, as shown in Figure 3.5-9.

For the small flow phase, some differences in cavitation factors between scales are apparent in Figure 3.5-9 at large cavitation factors (Case 6). Small Flow CFD employs a flow inlet boundary condition for solution stability, and calculates an inlet pressure. Differences in the cavitation factors for small flow are caused by differences in the calculated inlet pressure. These larger differences are caused by a larger numerical mesh uncertainty in Case 6 at larger cavitation factors for small flow injection, which is represented using the Grid Convergence Index (GCI) as described later. The uncertainty due to the large GCI is appropriately taken into account in LOCA safety calculations.

The scale effect is illustrated by Figure 3.5-10 with the abscissa of scale and the ordinate of the  $C_v$  value. The figure shows that relative differences of  $C_v$  of small flow are larger than that of large flow. However, the scale effects of  $C_v$  appear to be small. The scale effect quantified by CFD (i.e., CFD-Evaluated Scale Effect), between 1/2 and 1/1 scale is described in section 3.5.3 in detail.





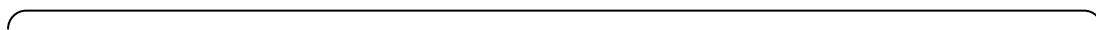
**Figure 3.5-7(a) Flow Structure in Vortex Chamber (Case 3 Large Flow 5 sec)**





Figure 3.5-7(b) Flow Structure in Outlet Nozzle (Case 3 Large Flow 5 sec)





**Figure 3.5-8(a) Flow Structure in Vortex Chamber (Case 3 Small Flow 43 sec)**



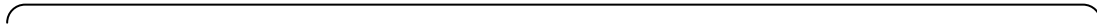


**Figure 3.5-8(b) Flow Structure in Outlet Nozzle (Case 3 Small Flow 43 sec)**





**Figure 3.5-9 Comparison between 1/2 and 1/1 Scale of CFD Result**



**Figure 3.5-10(a) Relationship between Flow Rate Coefficient and Scale (Large Flow)**

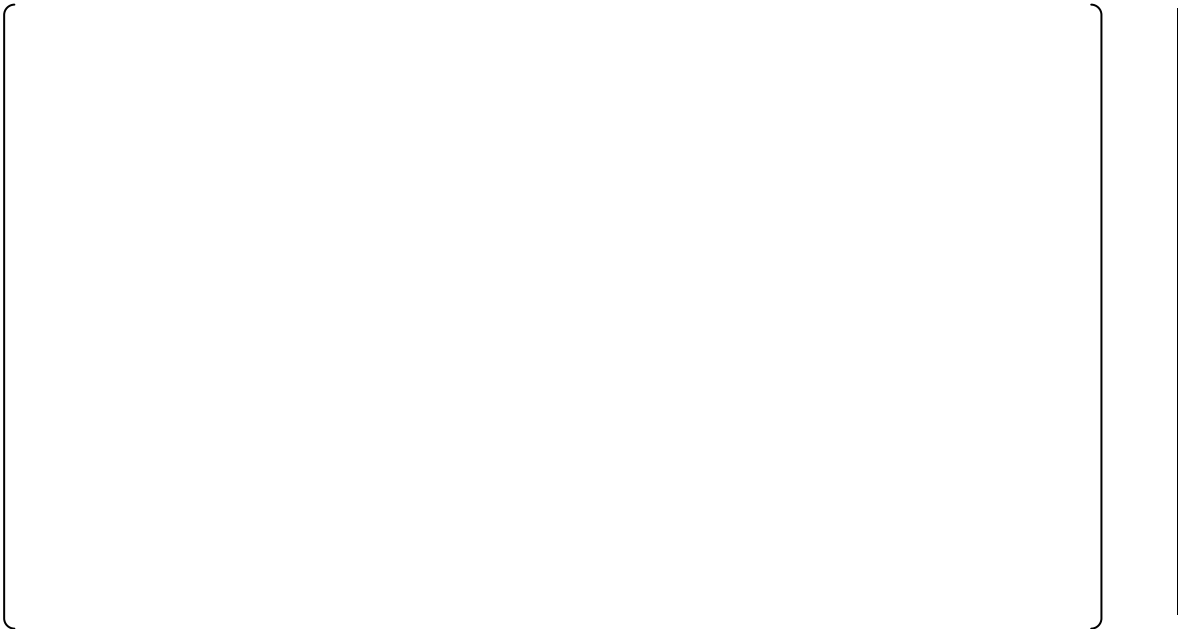


**Figure 3.5-10(b) Relationship between Flow Rate Coefficient and Scale (Small Flow)**

### 3.5.3 Evaluation of Scale Effect between 1/2 and 1/1 scale

#### (1) Outline

The scale effect and its uncertainties obtained from the difference of CFD results between the 1/2 and 1/1 scale models are referred to as the “CFD-Evaluated Scale Effect” and are shown in this section.

#### (2) Scale Effect and Uncertainty

Possible scale effects between the 1/2 and 1/1 scale models are quantified from the CFD results for the 1/2 and 1/1 scale ACCs.

CFD-Evaluated Scale Effects between the 1/2 and 1/1 scale models are considered to be represented by an average of the calculated values and an uncertainty (i.e., dispersion) related to the calculated values. The average value is considered to be a bias error. The uncertainty in the mean value (bias error) may arise from two sources:

- Dispersion of the mean ( $u_{SD}$ ) from the calculated values of the scale effect at each analyzed test case / time point.
- Propagation of uncertainty ( $u_{mesh}$ ) in each calculated value of the scale effect from the numerical uncertainty in every 1/2 and 1/1 scale CFD result.

Therefore, the CFD-Evaluated Scale Effects are defined by the following expressions.

$$\begin{aligned} \text{CFD-Evaluated Scale Effects} &\approx (Cv_{1/1} - Cv_{1/2}) / Cv_{1/2} && \text{Eq. 3.5.3-1} \\ &\rightarrow \delta Cv_{scale} \pm u_{scale} \\ &(\text{statistical representation}) \end{aligned}$$

$\delta Cv_{scale}$  : Scale effect bias estimated from CFD results  
(Scale effect bias is evaluated from the average, because  $Cv_{1/1}$  and  $Cv_{1/2}$  have a numeric error margin respectively.)

$u_{scale}$  : Standard ( $1\sigma$ ) uncertainty of the scale effect bias estimated from CFD results

$$[ \quad \quad \quad ] \quad \quad \quad \text{Eq. 3.5.3-2}$$

Each of the uncertainty components is considered to be normally (Gaussian) distributed, such that  $u_{scale}$  is calculated by the square root sum of squares as defined by the following expressions.

$$u_{\text{scale}}^2 = u_{\text{SD}}^2 + u_{\text{mesh}}^2 \quad \text{Eq. 3.5.3-3}$$

$$u_{\text{SD}} = C_{T,95}(n) / 1.96 \times \text{S.D.} \quad \text{Eq. 3.5.3-4}$$

(1 $\sigma$  standard uncertainty calculated from a two-sided 95% probability, based on limited number of results)

$$u_{\text{mesh}} = \text{Evaluated by GCI (Grid Convergence Index)} \\ \text{(The expression is described below in Section 3.5.3(3).)}$$

$u_{\text{SD}}$  : Standard (1 $\sigma$ ) uncertainty due to deviation from bias

$u_{\text{mesh}}$  : Standard (1 $\sigma$ ) uncertainty due to spatial discretization approximation for CFD calculations (GCI)

M.V. : Mean value of differences between 1/2 and 1/1 scale CFD

S.D. : Standard deviation of differences between 1/2 and 1/1 scale CFD

N : Number of data pairs (1/2 and 1/1 scale CFD cases)

$C_{T,95}(n)$  : Factors for tolerance interval to contain at least 95% of population (Table 3.5-2) (According to the "Test Uncertainty" (Ref.16))  
The validity of using  $C_{T,95}(n)$  is described in Appendix-H.

$Cv_{1/1,i}$  : Flow rate coefficient in case i obtained by CFD for 1/1 scale ACC

$Cv_{1/2,i}$  : Flow rate coefficient in case i obtained by CFD for 1/2 scale ACC



**Table 3.5-2 Factors for Calculating the Two-Sided 95% Probability Intervals for A Normal Distribution (Ref.16))**

Number of Given Observations	Factors for Tolerance Interval to Contain at Least 95% of the Population
n	$C_{T,95}(n)$
4	6.37
5	5.08
6	4.41
7	4.01
8	3.73
9	3.53
10	3.38
11	3.26
12	3.16
15	2.95
20	2.75
25	2.63
30	2.55
40	2.45
60	2.33
$\infty$	1.96

### (3) GCI Uncertainty

According to the “ASME V&V 20-2009” (Ref.8), GCI can be understood as,

- Uncertainty of the solutions derived from discretized equations by a numerical and analytical approach.
- Its uncertainty is at 95% confidence level, and that is consistent with the 1.96 sigma range for a Gaussian distribution.

On page 11 of ASME V&V 20-2009, it states,

*“uncertainty estimate  $U_{x\%}$  is intended to provide a statement that the interval  $f \pm U_{x\%}$  ( $f$  is numerical solution) characterizes a range within which the true (mathematical) value of  $f_t$  falls, with probability of  $x\%$ .”*

Also on page 12 of ASME V&V 20-2009, it states,

*“The GCI is an estimated 95% uncertainty obtained by multiplying the absolute value of the (generalized) RE error estimate (or any other ordered error estimator) by an*

*empirically determined factor of safety,  $F_s$ . The  $F_s$  is intended to convert an ordered error estimate into a 95% uncertainty estimate.”*

- Numerical uncertainty ( $u_{\text{mesh}}$ ) is evaluated using GCI, which is defined as a ~95% confidence interval for the numerical error.
- For the purpose of combining with other uncertainties (i.e., coverage factors for converting expanded uncertainty to standard uncertainty), the GCI is assumed to be a normal Gaussian distribution (i.e., 95% coverage =  $1.96\sigma$ ).
- Numerical uncertainty ( $u_{\text{mesh}}$ ) in the calculation of the CFD-Evaluated Scale Effect is a standard uncertainty ( $1\sigma$ ) estimated by dividing the GCI (95% coverage) by 1.96.
- For simplicity, the maximum value of the combined GCI at each evaluated point is used.

$u_{\text{mesh}}$  is defined by the following expressions.

$$\left[ \begin{array}{c} \text{ } \\ \text{ } \end{array} \right] \quad \text{Eq. 3.5.3-5}$$

#### (4) Results

The evaluated scale effect is shown in Tables 3.5-3 and 3.5-4. The results for the large and small flows with standard ( $1\sigma$ ) uncertainties are [                      ] % and [                      ] %, respectively.

**Table 3.5-3 Uncertainties in ACC Flow Model (Large Flow)**

**Table 3.5-4 Uncertainties in ACC Flow Model (Small Flow)**

$u_{scale}$  for the small flow is relatively large compared to that for the large flow, due to the relatively larger GCI values in the CFD results for the small flow. The larger GCI values are a result of the complicated flow field in the vortex behavior occurring during small flow, which requires a higher grid resolution to accurately model. In the small flow condition, the velocity gradient is stronger than that in the large flow as shown in Figures 3.5-7 and 3.5-8. This complicated flow field requires more grid resolution to capture the flow behavior accurately. However, the current CFD results and grid resolution are considered to be adequate for evaluating the scale effect, since the numerical uncertainty (even for the small flow) is relatively small compared to the uncertainties due to the instrumentation and experimental dispersion described in Reference 1.

As discussed in Appendices B and C, the primary models in the CFD possess an ability to evaluate the scale effect in the hydraulic behaviors dominating the accumulator flow rate. Although the numerical uncertainty is a large component of the CFD-Evaluated Scale Effect, in particular for the small flow, the present CFD analyses demonstrate that the scale effect for the accumulator flow rate is small.

## 4.0 CONCLUSIONS

The topical report (Ref. 1) discussed the scaled model testing and development of the characteristic equation for the hydraulic performance of the 1/2 scaled, full-height, ACC model. Reference 1 also discussed the governing flow phenomena and scalability concerns to conclude that the scale effect in applying the 1/2 scale ACC hydraulic performance to the 1/1 scale ACC is expected to be small.

This technical report performed steady-state CFD analyses implemented in FLUENT for the 1/2 scale and 1/1 scale analytical models. Conditions for the CFD calculation include both large and small flow injections for a wide range of cavitation factors. The results demonstrate the similarity of the flow characteristics and support the validity of the conclusion described in the topical report, and also provide quantitative evaluations of the scale effect using CFD for application to the characteristic equations for the 1/1 scale ACC hydraulic performance.

Conclusions of the CFD results and the evaluations are shown below:

- The 1/2 scale ACC CFD analysis shows similar flow structure to the expected conceptual flow in the flow damper.
- The CFD analyses are applicable for evaluations of large and small flow injections. In the 1/2 scale ACC analysis, the correlation between  $C_v$  and  $\sigma_v$  was reasonably consistent with the measured data, showing that CFD is applicable to estimate the scale effects in the ACC
- CFD calculations provided a good similarity for the flow structure in the flow damper and in the injection piping between the 1/2 and 1/1 scale ACCs.
- The scale effect bias for the characteristic equations is quantified by comparing the CFD calculation results for both the 1/2 and 1/1 scale ACC, which showed that the average scale effect bias is small compared to the experimental uncertainties.
- The CFD-Evaluated Scale Effect, which includes the uncertainty in the scale effect bias calculated through CFD analyses, is quantified for application to the characteristic equations for 1/1 scale ACC hydraulic performance.

## 5.0 REFERENCES

- 1) Topical Report “The Advanced Accumulator”, MUAP-07001 Revision 3
- 2) Large Break LOCA Code Applicability Report for US-APWR, MUAP-07011 Revision 1
- 3) ANSYS FLUENT, FLUENT 12.0 Documentation, User's Guide and Validation Guide
- 4) Roache, P.J. (1994), Perspective : A Method for Uniform Reporting of Grid Refinement Studies, Journal of Fluids Engineering, Vol.116, pp.405-413
- 5) Best Practice Guidelines for the Use of CFD in Nuclear Reactor Safety Applications, NEA/CSNI/R(2007)5
- 6) Celik, I.B., Ghia, U., Roache, P.J. and Freitas, C.J., Procedure for Estimation and Reporting of Uncertainty Due to Discretization in CFD Applications
- 7) Statement on the Control of Numerical Accuracy, Journal of Fluids Engineering Editorial Policy
- 8) Standard for Verification and Validation in Computational Fluid Dynamics and Heat Transfer, ASME V&V 20-2009
- 9) T. Watanabe, T. Kawamura, Y. Takekoshi, M. Maeda, S.H. Rhee, Simulation of steady and unsteady cavitation on a marine propeller using a RANS CFD code, Fifth International Symposium on Cavitation, Osaka, Japan, November 2003
- 10) CFD Simulation of Flow in Vortex Diodes, AIChE Journal, Vol.54, No.5, P1139-1152, May 2008
- 11) A.K. Singhal, M.M Athavale, H. Li, Y. Jiang, Mathematical Basis and Validation of the Full Cavitation Model, Journal of Fluids Engineering, Vol. 124, PP 617 – 624, September 2002
- 12) P.J. Zwart, A.G. Gerber, T. Belamri, A Two-phase Flow Model for Predicting Cavitation Dynamics, ICMF 2004 International Conference on Multiphase Flow, Yokohama, Japan, May 2004
- 13) G.H. Schnerr, J. Sauer, Physical and Numerical Modeling of Unsteady Cavitation Dynamics, 4th International Conference on Multiphase Flow, New Orleans, USA, May 2001
- 14) TRAC-M/FORTRAN 90(version 3.0) theory manual, LA-UR-00-910, J.W. Spore, pp F- 13, July 2000
- 15) Best Practice Guideline for the CFD Simulation of Flows in the Urban Environment APPENDIX A, COST Action 732, 1 May 2007,
- 16) Test Uncertainty, ASME PTC 19.1-2005(Revision of ASME PTC 19.1-1998)
- 17) S. Huang, M. He, C. Wang and X. Chang, Simulation of Cavitating Flow Around a 2-D Hydrofoil, Journal of Marine Science and Application, Vol. 9, No. 1, pp 63-68, 2010

- 18) M. Dular, R. Bachert, B. Stoffel, B. Sirok, Experimental Evaluation of Numerical Simulation of Cavitating Flow Around Hydrofoil, European Journal of Mechanics B/Fluids, Vol. 24, pp 522-538, 2005
- 19) Andreas P. Keller, Hubert K. Rott, The Effect of Flow Turbulence on Cavitation inception, ASME Fluids Engineering Division Summer Meeting FEDSM 97 June 22-26, 1997.

|

## Appendix-A

### Calculation of GCI

To estimate the spatial discretization errors in the CFD model, Roache introduced the Grid Convergence Index (GCI, Ref.4). This appendix describes the GCI calculation procedure and provides the results for the ACC CFD analyses.

GCI is calculated as shown in the following steps (Ref.5 to Ref.8 and Ref.15).

#### Step 1.

Define a representative cell, mesh or grid size  $h$ . For three dimensional calculations,

$$h = \left( \frac{1}{N} \sum_{i=1}^N (\Delta V_i) \right)^{1/3} \quad \text{Eq. A1}$$

where

$\Delta V_i$  is the volume and  $N$  is the total number of cells used for the computations.

For the ACC evaluation, the total number of cells is based on the mesh of the Standpipe, Vortex Chamber, Outlet Nozzle and Injection Pipe.

#### Step 2.

Select three significantly different sets of grids, and run simulations to determine the value of key variables important to the objective of the simulation study ( $\phi$ ).

It is recommended that the grid refinement factor,  $r = h_{\text{coarse}} / h_{\text{fine}}$ , be greater than 1.1 (Ref.4). This value of 1.1 is based on experience, and not on formal derivation.

#### Step 3.

Let  $h_1 < h_2 < h_3$  and  $r_{21} = h_2 / h_1$ ,  $r_{32} = h_3 / h_2$ , and calculate the apparent order,  $p$ , of the method using the expression,

$$p = \frac{1}{\ln(r_{21})} \left| \ln |\varepsilon_{32} / \varepsilon_{21}| + q(p) \right|, \quad \text{Eq. A2}$$

$$q(p) = \ln \left( \frac{r_{21}^p - s}{r_{32}^p - s} \right), \quad \text{Eq. A3}$$

$$s = 1 \cdot \text{sign}(\varepsilon_{32} / \varepsilon_{21}) \quad \text{Eq. A4}$$

where



$$\varepsilon_{32} = \phi_3 - \phi_2, \varepsilon_{21} = \phi_2 - \phi_1, \phi_k \text{ denoting the solution on the } k^{\text{th}} \text{ grid.}$$

Here, parameter “s” (Eq. A4) is the indicator of “Oscillatory Convergence”. If “s = 1”, that means the grid convergence under consideration is monotonic. On the other hand, if “s = -1”, that means the grid convergence is oscillatory. By considering “s” in Eq.A3, this calculation procedure provides GCI even if the grid convergence under consideration has oscillatory convergence characteristics.

#### Step 4.

Calculate the extrapolated values from

$$\phi_{ext}^{21} = (r_{21}^p \phi_1 - \phi_2) / (r_{21}^p - 1). \quad \text{Eq. A5}$$

#### Step 5.

Calculate and report the following error estimates, along with the apparent order of  $p$  :

Approximate relative error:

$$e_a^{21} = \left| \frac{\phi_1 - \phi_2}{\phi_1} \right| \quad \text{Eq. A6}$$

Extrapolated relative error:

$$e_{ext}^{21} = \left| \frac{\phi_{ext}^{21} - \phi_1}{\phi_{ext}^{21}} \right| \quad \text{Eq. A7}$$

The fine-grid convergence index:

$$\text{GCI}_{\text{fine}}^{21} = \frac{Fs \cdot e_a^{21}}{r_{21}^p - 1} \quad \text{Eq. A8}$$

The guideline for the selection of “ $F_s$ ” (Ref.15)) is as follows:

For  $F_s$ , Roache suggests two values depending on the number of grids used and on the relation of the apparent (observed) and formal order of accuracy:

- $F_S = 1.25$  if the order of accuracy is calculated from solutions on three grids and this observed order matches the formal one.
- $F_S = 3$  if only two grids are used, i.e. the observed order is assumed to match the formal one, or if three grids are used but the observed and formal order do not match.

By following the steps shown above, GCI values are calculated. Here, the variable to be evaluated ( $\phi$ ) is flow rate coefficient  $C_v$ , and tank pressure  $P_g$ .

Figure A-1 to A-3 show the series of grids which are used for the GCI evaluations for the ACC.

Table A-1 and A-2 show the GCI calculation procedure for  $C_v$  and its evaluation results for 1/2 scale and 1/1 scale, respectively. Similarly, Table A-3 and A-4 are for  $P_g$ , however on only some of small flow condition cases (CASE3-43 sec, and CASE6-82 sec).

Figure A-4 and A-5 show the representative grid convergence trend curve ( $C_v$  and  $P_g$ ) for 1/2 scale and 1/1 scale, respectively.



Large Flow 1/2 Scale    Large Flow 1/1 Scale    Small Flow 1/2 Scale    Small Flow 1/1 Scale  
**Figure A-1 CFD Mesh Configurations (Fine Mesh)**



Large Flow 1/2 Scale    Large Flow 1/1 Scale    Small Flow 1/2 Scale    Small Flow 1/1 Scale  
**Figure A-2 CFD Mesh Configurations (Normal Mesh)**



Large Flow 1/2 Scale    Large Flow 1/1 Scale    Small Flow 1/2 Scale    Small Flow 1/1 Scale

**Figure A-3 CFD Mesh Configurations (Coarse Mesh)**

**Table A-1 Calculation Procedure of GCI for 1/2 Scale Model CFD**  
**( $\phi$  = Flow Rate Coefficient Cv)**

**Table A-2 Calculation Procedure of GCI for 1/1 Scale Model CFD**  
**( $\phi$  = Flow Rate Coefficient Cv)**


In regard to the observed p values, the calculation results show a relatively higher order of convergence than the expected theoretical value of approximately 2 or lower (due to the 2<sup>nd</sup> order and 1<sup>st</sup> order accurate scheme in these calculations). The discretization errors are highly grid dependent, and the grid refinement ratio “r” applied in these calculations is not fine enough to resolve the grid convergence trend curve. However, since grid convergence proceeds so quickly (i.e. observed p is large), the final fine-mesh values are sufficiently converged to reduce discretization error and the larger Fs value (i.e. 3) is employed conservatively.

**Table A-3 Calculation Procedure of GCI for 1/2 Scale Model CFD**  
( $\phi$  = Tank Inlet Pressure  $P_g$  (Mpa, abs))

--

**Table A-4 Calculation Procedure of GCI for 1/1 Scale Model CFD**  
( $\phi$  = Tank Inlet Pressure  $P_g$  (Mpa, abs))

--



**Figure A-4 Representative Grid Convergence Trend Curve  
for  $C_v$  (Flow Rate Coefficient) and  $P_g$  (Tank Pressure)  
with 1/2 Scale Model**



**Figure A-5 Representative Grid Convergence Trend Curve  
for  $C_v$  (Flow Rate Coefficient) and  $P_g$  (Tank Pressure)  
with 1/1 Scale Model**



**Appendix-B****Scale-up Capability of Turbulence Model**

The purpose of Appendix-B is to show that the generalized turbulence model applied to this CFD can be used to evaluate the scaling effect. First, the general RSM model and its scale-up capability is discussed. Next, the methodology and basis for tuning the RSM model to better predict the specific flow fields for the ACC are described. Finally, the results of sensitivity calculations performed with the tuned RSM model are presented to demonstrate that the CFD-Evaluated Scale Effect calculated with the generalized RSM model are suitable.

**B-1. Introduction**

The small flow results described in the body of this report demonstrate a larger amount of deviation from the observed test results than the large flow results. Although the CFD-Evaluated Scale Effect is a differential calculation, this appendix evaluates the impact of the (absolute) deviation from the observed test results.

The important physical process models applied in this CFD simulation are the cavitation model and the turbulence model. The present calculation simulates high speed U-shaped flow and flow through an outlet nozzle under large flow conditions, and simulates strong swirling flow under small flow conditions. The difference in  $C_v$  between the CFD result and test data is about [ ] under large flow conditions which is within the test instrument error and considered acceptable as discussed in Appendix-J.

For small flow, the comparison error is about [ ]. Cavitation does not occur under small flow conditions analyzed in the body of this report. Thus, the cavitation model is not the source of this comparison error. The  $C_v$  approaches an asymptotic numerical value as the grid is refined. The current mesh structure is fine enough to provide numerically accurate simulation results (See Appendix-A).  $Y^+$  in the current calculation grid is less than 300 as shown in Appendix-G, as the grid point near the wall should be located within the log-law layer. Thus it is believed that the effect of the boundary layer can be adequately evaluated under the current grid configuration.

These relatively large distortions under the small flow conditions are mainly caused by the RSM turbulence model (discussed in Item 3 below), which has been applied to predict the strong swirling flow inside the vortex chamber. The CFD simulation predicts smaller  $C_v$  under the small flow conditions. The current CFD model tends to predict stronger swirling/vortex in the Vortex Chamber than in the test.

The Navier-Stokes equation is the governing equation that represents fluid behavior. Reynolds stress can be obtained by applying “Reynolds averaging” to the Navier-Stokes equation (RANS). However, these simplified methods are typically not recommended for three-dimensional or swirling flows with large directional changes. The ACC CFD analysis uses the Reynolds Stress Model (RSM) turbulence model which describes the Reynolds stress with the transport equation. RSM consists of a pressure-strain correlation term, diffusion term, and viscous dissipation term in the transport equation for Reynolds stress. Constants in these models/correlations have been optimized by using a wide variety of experimental data for fundamental turbulent flow and DNS (direct numerical simulation) databases. For this reason, RSM error should be independent of scale.

The RSM model error is independent of scale, for the same type of flow. The model error is due to the type of flow (specific ACC application of swirling flow versus a generalized “one-size-fits-all” RSM model), not the scale of the flow. Therefore, the model error from the RSM model should be the same for 1/2 scale and 1/1 scale. For these complex phenomena, especially for strong swirling flow under the small flow mode, the absolute accuracy of the CFD is reduced. However, the RSM applied here is based on the governing equation of fluid flow and its applicability has been verified for a wide range of flow conditions. The model is sufficiently applicable to evaluate degrees of sensitivity between two cases as is done for the evaluation of the scale effect.

The difference between the tests results and CFD results in the current CFD model (in the body of this report) for small flow are expected to be due to the application of the generalized RSM model to the specific strong swirling flow in the ACC. This error is not expected to significantly affect the CFD-Evaluated Scale Effect calculated between scales.

## B-2 Turbulent Model Tuning to Lessen Model Error

Compared to the test data, CFD simulation predicts an approximately [ ] smaller flow rate coefficient  $C_v$  under the small flow conditions. This model error is larger than the uncertainty of the test data. The characteristic of small flow is the strong swirl flow in the vortex chamber and it is well-known that the standard turbulent model cannot predict the flow characteristics, especially the velocity distribution. This section describes the methodology for tuning the turbulent model to reduce the absolute model error for the ACC flow field.

### B-2-1 General Methodology

Under small flow conditions, the  $C_v$  value obtained from the CFD calculation was [ ] smaller than the  $C_v$  value obtained from the experiment. Therefore, CFD overestimates the flow resistance. Flow resistance under the small flow condition is dominated by the strong swirl flow in the vortex chamber. This suggests that the CFD overestimates the strength of the swirl flow in the vortex chamber. The model error of CFD is causally-related to this overestimation.

The characteristics of the turbulence in the swirling flow are anisotropic in nature. For this reason, the Reynolds Stress Model (RSM), which can independently solve for and evaluate the anisotropic flows, is most suitable for simulating the swirl flow. Therefore, RSM is applied to this calculation.

In the RSM, the rigorous Reynolds stress equations generated by applying the Reynolds decomposition ( $u = \bar{u} + u'$ ,  $\bar{u}$ : time average velocity component,  $u'$ : fluctuating velocity component) to the velocity in the Navier-Stokes equations and applying the ensemble average to this equation are solved. In the default RSM model, coefficients in the modeled Reynolds stress equations have been tuned based on experimental data. The RSM has a dissipation rate,  $\varepsilon$ , which is the unknown variable, and an equation relating to  $\varepsilon$  is required for solving the equation system. Therefore in the turbulent model, the transport equation for  $\varepsilon$ , which is derived from the transport equation of turbulent kinetic energy,  $k$ , by multiplying both sides of the  $k$ -equation by  $(\varepsilon/k)$ , is used for closing the equation system as shown below.

$$\frac{\partial(\rho\varepsilon)}{\partial t} + \frac{\partial}{\partial x_i}(\rho\varepsilon u_i) = \frac{\partial}{\partial x_i} \left[ \left( \mu + \frac{\mu_t}{\sigma_\varepsilon} \right) \frac{\partial \varepsilon}{\partial x_i} \right] + C_{\varepsilon 1} \frac{1}{2} [P_{ii} + C_{\varepsilon 3} G_{ii}] \frac{\varepsilon}{k} - C_{\varepsilon 2} \rho \frac{\varepsilon^2}{k} + S_\varepsilon$$

The RSM uses this  $\varepsilon$  transport equation. But as previously explained, the  $\varepsilon$  equation is not derived from the physical model. For this reason, the coefficients included in this equation ( $C_{\varepsilon 1}, C_{\varepsilon 2}$ ) are the parameters which could be tuned to optimize the equation system for a specific type of flow. It is recommended that these coefficients should be set for predicting the intended experiment datum. In Reference B-1) and B-2), a similar definition can be

shown. It is clear that tuning for a specific flow field been applied widely, and many researchers have performed tuning of the  $\varepsilon$  equation as shown in Table B2-1.

**Table B2-1 Examples of Tuning the  $\varepsilon$  Equation** (Ref. B-3))

Model	$C_\varepsilon$	$C_{\varepsilon 1}$	$C_{\varepsilon 2} f_2$	Additional term	$C_{\varepsilon 3}$
Hanjalić & Launder (1976)	0.15	$C_{\varepsilon 2} - 3.5C_\varepsilon$	$1.8[1 - \frac{0.4}{1.8} \exp\{-(R_t/6)^2\}]$	$4.0C_{\varepsilon 3} \nu \frac{(\overline{uv})^2}{\varepsilon} (\overline{U}_{,yy})^2$	2.0
Prud'homme & Elghobashi (1983)	$0.15f_\mu$	1.45	$1.9[1 - 0.263 \exp\{-R_t^2/36\}]$	$2\nu \frac{k}{\varepsilon} f_\mu \overline{v^2} (\overline{U}_{,yy})^2$	
Kebede et al. (1985)	0.18	$1.45(1 - f_s) + 2.0f_s$	1.9	$C_{\varepsilon 3} \nu \frac{k}{\varepsilon} \overline{v^2} (\overline{U}_{,yy})^2$	0.3
Shima (1988)	0.15	$1.35(1 + f_w)$	1.8	$\xi$	
Launder & Shima (1989)	0.18	$1.45 + \psi_1 + \psi_2$	1.9	No additional term	
Lai & So (1990)	0.15	$1.35(1 + \sigma f'_w)$	$1.8[1 - \frac{2}{9} \exp\{-(R_t/6)^2\}]$	$\xi'$	
Shih (1990)	0.07	$1.05 \frac{\varepsilon}{\varepsilon}$	$\psi_0/2$	$C_{\varepsilon 3} \nu \frac{k}{\varepsilon} \overline{v^2} (\overline{U}_{,yy})^2$	$0.3(1 - F)$
Launder & Tselepidakis (1992)	0.18	1.0	$\frac{1.92}{1 + 0.63[F(-8\Pi)]^{0.5}}$	$2C_{\varepsilon 3} \nu (k/\varepsilon) \overline{v^2} (\overline{U}_{,yy})^2 + (0.92 \times 2\nu \frac{\varepsilon}{k} k_{,y})_{,y}$	0.43

An example of tuning the normal RSM in FLUENT performed by Laundar, Reece, Rodi<sup>(Ref B-4)</sup> is shown in Figure B2-1. This example shows the calculation result of the swirl flow in the rotating pipe around the pipe axis and a comparison between the calculated results and the experimental data. N represents the ratio between the axial velocity and the rotating velocity and increasing N implies a stronger swirl. The flow distribution shape changes as the swirl flow becomes stronger. The RSM can represent the overall behavior (i.e., general shape) of the change in velocity distribution. However, the deviation between the measured results and the calculation results becomes larger as the swirling becomes stronger. That is, RSM accurately predicts general trends for swirling turbulent flow and would be suitable for a differential analysis. However, the (absolute) deviation between the experimental data and calculation results becomes larger for stronger swirling flow.

There is a study by Prof. Shima<sup>(B-6))</sup> for developing the RSM which can be applied to flow with a strong anisotropic nature. In this study,  $C_{\varepsilon 2}$  was kept constant because the tuning of  $C_{\varepsilon 2}$  performed by Lumley did not generate good results. However, by tuning the  $C_{\varepsilon 1}$  coefficient, the velocity distribution of the swirling flow could be predicted adequately.

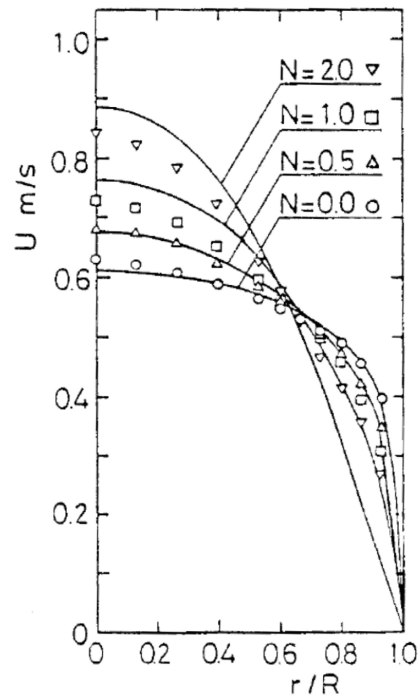


**Figure B2-1 Axial Velocity Distribution of the Swirling Flow  
in the Rotating Pipe around the Pipe Axis** (Ref. B-5))

By tuning  $C_{\varepsilon 1}$ , which can be adjusted in FLUENT, the velocity distribution of the swirling flow can be adjusted to better match the observed Cv value from 1/2 scale testing. MHI determined that changing the default value of  $C_{\varepsilon 1} = 1.44$  to [ ] sufficiently reduced the deviation from the test values over the range of cases analyzed. Although the coefficient of the equation can be tuned for this target flow field (swirling flow in vortex chamber), the tuned value of the coefficient should not be applied to the general-purpose turbulent model for other types of flow since this tuning is a limited adjustment for the specific ACC small flow conditions.

To validate the tuned  $C_{\varepsilon 1}$  value, additional calculations were performed for comparison to the 1/2-scale small flow test data.

- a) To address any dependency on velocity, two calculation cases each were performed with the tuned  $C_{\varepsilon 1}$  value for both high velocity conditions and low velocity conditions (four total). Comparing the Cv value between the calculation and the experiment, the difference between the calculation and experiment decreases and falls within the experimental uncertainty.
- b) Qualitatively, the velocity and pressure distribution patterns were reviewed for general consistency with the results expected from the general RSM model.

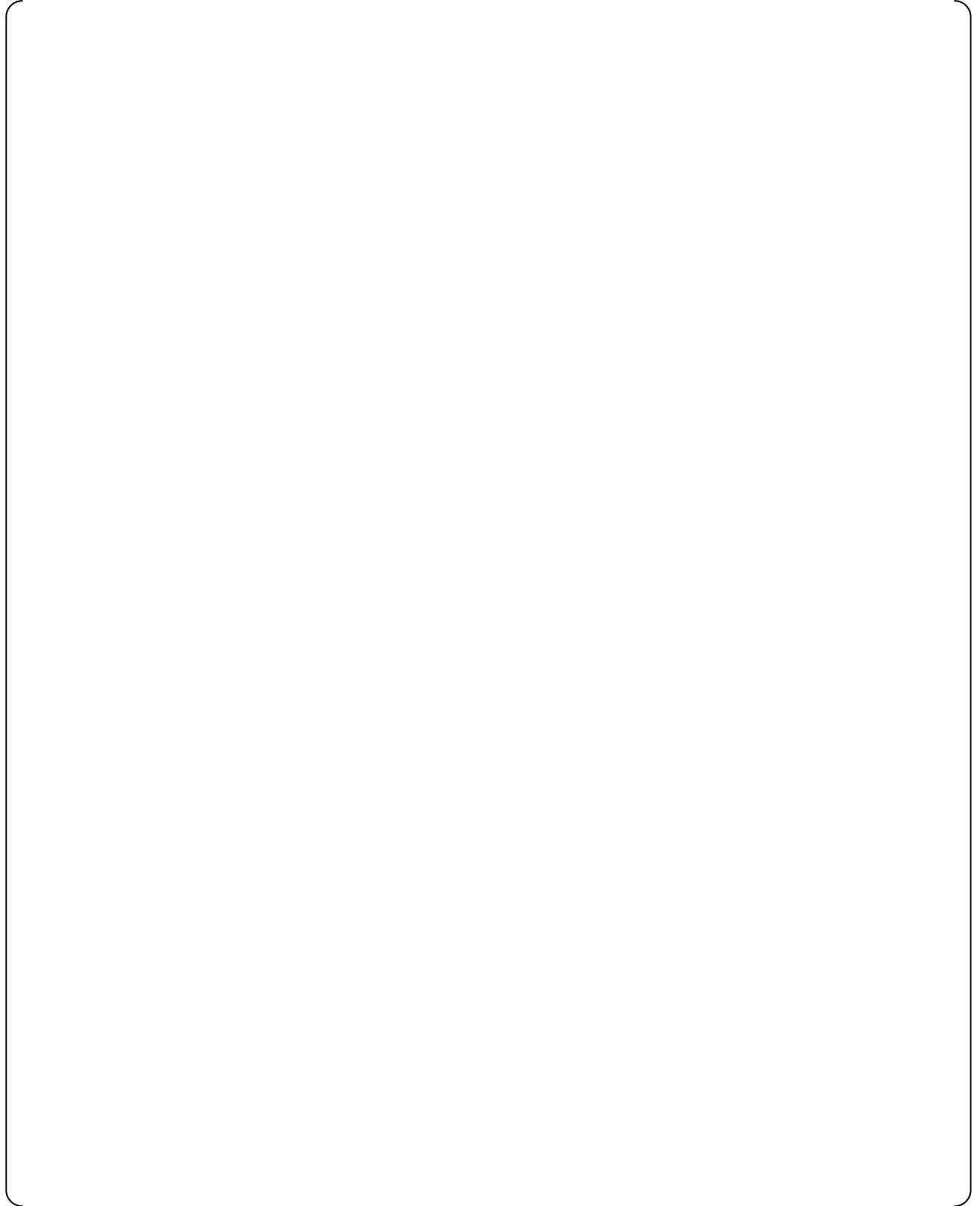
As discussed above, the model error between the CFD result and the experimental result falls within the experimental uncertainty range by applying this tuning.

### **B-3 RSM Model Tuning for ACC**

The overlap between test results and calculation results for flow rate coefficient are plotted in Figure B3-1 and B3-2. For large flow CFD results, the calculated  $C_v$  values are plotted within the measurement error bar. Detailed comparisons are shown in Appendix-J.

With the current empirical constants in the RSM model, the magnitude of the comparison error (i.e. the difference between the test value and the calculated value) in the  $C_v$  value is large and outside the range of instrument uncertainty for the small flow condition. To reduce the comparison error in the small flow condition to within instrument uncertainty, the RSM model coefficients are adjusted.

This section discusses the specific methodology for RSM tuning for the ACC, validates the tuning by comparing to the 1/2 scale test data, and estimates the impact on the CFD-Evaluated Scale Effect.



### B-3-1 Methodology for ACC RSM Model Tuning

The current turbulence model tends to predict lower dissipation in the strong swirling/vortex field. As a result increasing the turbulent viscosity is necessary. Turbulent viscosity  $\mu_t$  is given in the formula below. Hence the turbulent kinetic energy  $k$  has to be increased and/or the turbulent energy dissipation rate  $\varepsilon$  has to be decreased.

$$\mu_t = \rho C_\mu \frac{k^2}{\varepsilon} \quad \text{Eq. B3-1}$$

RSM uses two equations:

- Reynolds stress equation: Derived analytically from the Navier-Stokes equation
- Turbulent dissipation equation ( $\varepsilon$ -equation): Assumed to be similar to the general transport equation and fit to empirical data

The turbulent dissipation equation is shown below:

Transport equation for turbulent energy dissipation rate

$$\frac{\partial(\rho\varepsilon)}{\partial t} + \frac{\partial}{\partial x_i}(\rho\varepsilon u_i) = \frac{\partial}{\partial x_i} \left[ \left( \mu + \frac{\mu_t}{\sigma_\varepsilon} \right) \frac{\partial \varepsilon}{\partial x_i} \right] + C_{\varepsilon 1} \frac{1}{2} [P_{ii} + C_{\varepsilon 3} G_{ii}] \frac{\varepsilon}{k} - C_{\varepsilon 2} \rho \frac{\varepsilon^2}{k} + S_\varepsilon \quad \text{Eq. B3-2}$$

$\varepsilon$	: Turbulent energy dissipation rate	$\rho$	: Density
$t$	: Time	$k$	: Turbulent kinetic energy
$x_i$	: Coordinate	$u_i$	: Velocity
$\mu$	: Viscosity coefficient	$\mu_t$	: Turbulent viscosity coefficient
$P_{ii}$	: Stress production term	$G_{ii}$	: Buoyancy production term
$S_\varepsilon$	: User - defined source term		
$\sigma_\varepsilon = 1.0 \quad C_{\varepsilon 1} = 1.44 \quad C_{\varepsilon 2} = 1.92$			

$C_{\varepsilon 3}$  is evaluated as a function of the local flow direction relative to the gravitational vector.

The coefficients in the equation are as follows:

- Coefficient  $C_{\varepsilon 1}$ : derived from the log-law condition of Universal Velocity Profile in turbulent flow. Default value is 1.44.
- Coefficient  $C_{\varepsilon 2}$ : derived from experimental data in homogeneous isotropic turbulent flow. So, hold the value as constant. Default value is 1.92.
- Coefficient  $C_{\varepsilon 3}$ : function of the velocity component to control the gravity effect.



As discussed in B-2, many researchers have refined the RSM coefficient by tuning  $C_{\varepsilon1}$ , and so MHI followed the same approach to reduce the difference between the test data and CFD result. The initial and final values are given below :

--

**B-3-2 Tuning Validation (Prediction Accuracy)**

After tuning, the comparison error of the Cv value becomes smaller than the uncertainty of the test data as shown in Table B3-1 and Figure B3-3. In all cases, model tuning increases the calculated Cv values, due to the decrease in turbulent energy dissipation in the tuned model. In addition, the tuned CFD model predicts the Cv values accurately within the measurement error bands of the test data. The mean differences from the measured data, both for the tuned and untuned models, are listed in Table B3-1, B3-2. An important observation is that the average bias between the calculation and measured data is largely improved in the tuned model, showing that the tuned model improves accuracy over the range of analyzed test cases. After tuning, the comparison error of the Cv value becomes smaller than the uncertainty of the test data as shown in Table B3-1 and Figure B3-3.

Table B3-3 shows the flow structure before and after tuning. The velocity and pressure distribution pattern in the vortex chamber is almost the same before and after tuning. No unexpected or unnatural flow appears by tuning.

In conclusion, the tuned CFD model has sufficient capability to reproduce the measured accumulator flow over the range of small flow injection conditions, and increased accuracy compared to the original model is being demonstrated. Thus, this tuning method can be applied.

**Table B3-1 Calculation Condition and Calculation Results Before and After Tuning  
for 1/2 Scale Model Calculation**

--

**Table B3-2 Effect of Tuning on Mean Cv Comparison Error (Small Flow)**

--	--

[illegible]

**B-3-3 RSM Tuning Results**

**(1) Influence on Scale Effect**

As shown in Figure B3-4, it can be confirmed that the scale effect obtained by the tuned turbulent model is almost the same as the scale effect obtained by the general model (before tuning).

**Table B3-4 Calculation Condition and Calculation Results Before and After Tuning for Scale Effect**



**Figure B3-4 Scale Effect for Cv by Tuning**

The sensitivity calculation cases analyzed include both the high and low velocity conditions over the range of test cases analyzed. Tuning of the RSM model results in a [     ] difference in the absolute value of Cv. However, as previously discussed, the CFD-Evaluated Scale Effect is a differential comparison of Cv values between scales. As Table B3-4 shows, the sensitivity study of the CFD model before and after tuning demonstrates that the impact on scale effect is significantly less.

## (2) Influence on Boundary Condition

In Appendix-D, it has been confirmed that the difference in the results using flow rate boundary versus using pressure boundary at the inlet is not significant in the untuned RSM model. In addition, boundary condition sensitivity calculations using the tuned CFD model are performed. The calculation results are shown in Table B3-5 and Table B3-6. These tables show that the difference in the applied boundary condition is negligible, similar to the conclusion using the untuned CFD model. Thus, the applicability of the flow rate boundary condition discussed in Appendix-D is confirmed for both the tuned and untuned RSM model.

However, as shown in Figure B3-3, since the tuned CFD increases the Cv value (i.e., decreases the inlet pressure) compared to the untuned CFD model, the tuned CFD model may lead to reduced the cavitation margin. The possibility of cavitation occurring during small flow for tuned CFD is discussed in Appendix-I.

### Table B3-5 Calculation Conditions of Tuned CFD

[illegible]

### Table B3-6 Calculation Results of Tuned CFD

**(3) Influence on GCI**

The influence of model tuning on the Grid Convergence Index (GCI) is evaluated through confirmatory calculations as follows.

The tuned GCI model is expected to be better than the GCI for the untuned model. The velocity profile in the vortex chamber is expected to become smoother through tuning by optimizing the energy dissipation in the strong swirling flow, thereby improving the grid convergence.

The expected grid convergence behavior with the tuned model is observed through the GCI results using the tuned model for the following small flow cases, which include both high and low velocity conditions:

- Case 3-43 sec, 1/2 Scale Model
- Case 3-43 sec, 1/1 Scale Model
- Case 6-82 sec, 1/2 Scale Model
- Case 6-82 sec, 1/1 Scale Model

GCI results with the tuned model are compared to the results for the untuned model in Table B3-7, and Grid Convergence trends are shown in Figures B3-5 and B3-6 which shows the results of Case 3-43 sec and Case 6-82 sec, respectively. The intermediate values for the GCI calculation for each case are shown in Table B3-8.

All calculation results indicate an improved GCI value by applying the tuned model. These results support the hypothesis about the grid convergence characteristics as discussed above, and it is concluded that the RSM model tuning provides better grid convergence in this case.

**Table B3-7 GCI Change Due to Tuning of Turbulence Model**

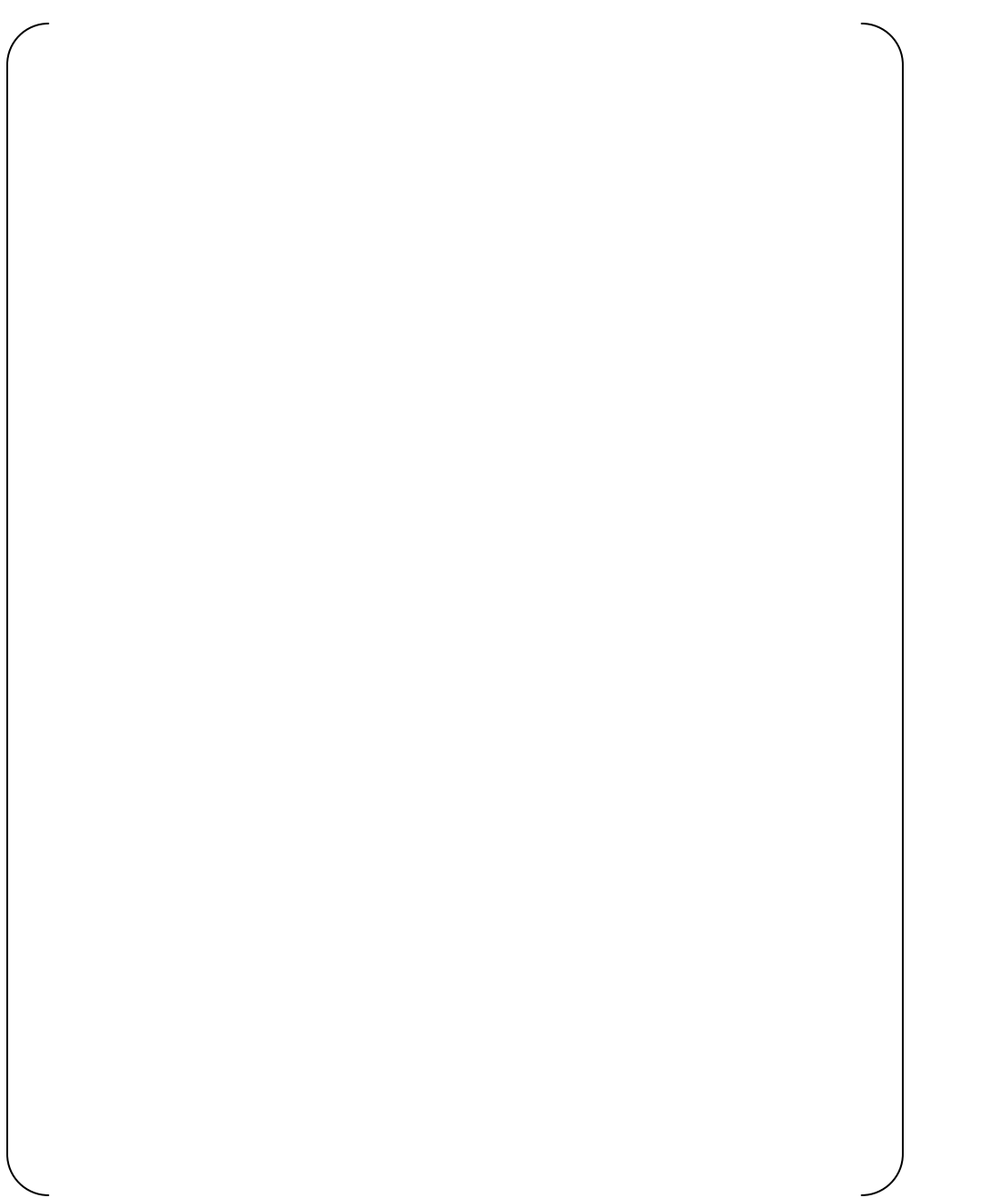


**Figure B3-5 Grid Convergence Trend Curve for “C<sub>v</sub>” for Case3-43 sec**

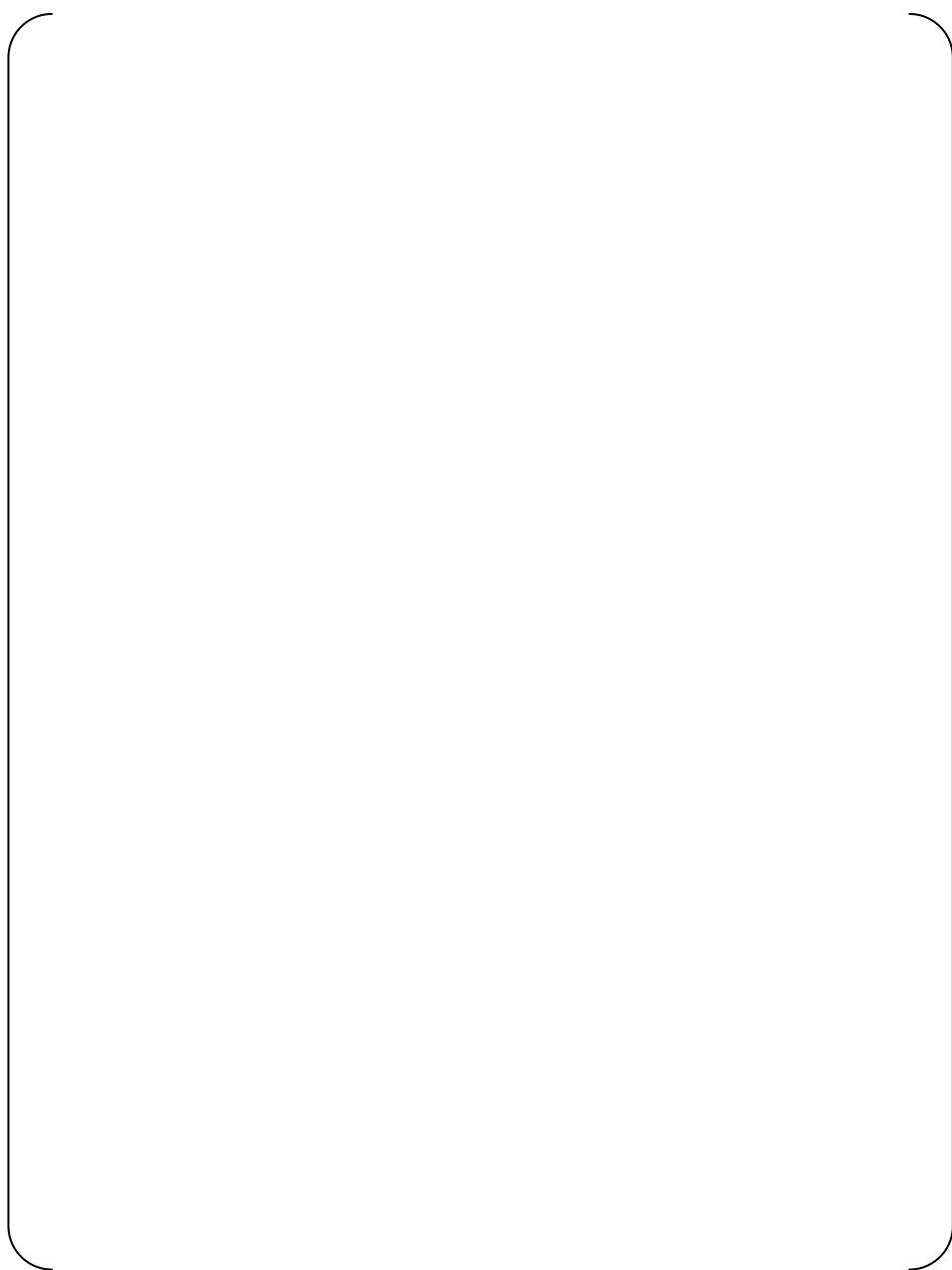


**Figure B3-6 Grid Convergence Trend Curve for “C<sub>v</sub>” for Case6-82 sec**



(a) High Velocity in Small Flow Condition, Case 3-43 sec

## B-4 Conclusions

Tuning of the RSM model to reduce the deviation between the small flow CFD results and the observed 1/2 scale test data was investigated. Tuning of the RSM model for specific flow fields has been performed by many researchers, and MHI followed a similar approach

The tuning method was validated by qualitatively comparing the velocity and pressure distributions and determining that no unexpected or unnatural flow conditions resulted from tuning. Quantitatively, the comparison error was shown to decrease and fall within the uncertainty of the test data for multiple test cases over a range of high and low velocity conditions.

The results of the RSM tuning for the ACC small flow conditions confirm the following:

- The scale effect obtained by the tuned turbulent model is approximately the same as the scale effect obtained by the current model (model before tuning).
- The turbulence tuning either does not have a significant influence on GCI (i.e. Grid Convergence Trend) or decreases the GCI.
- The RSM tuning is insensitive to boundary condition type, similar to general RSM model.

Therefore, re-evaluating with the tuned RSM model would reduce the CFD-Evaluated Scale Effect, mostly through reduced numerical uncertainty due to better grid convergence characteristics. Thus, the CFD-Evaluated Scale Effect calculated from the current turbulence model (model before tuning) is acceptable for use as a conservative bounding estimate of any actual scale effects between the 1/2 scale and full scale ACC.

## B-5 References

- B-1) Durbin, P.A., Pettersson Reif, B. A., "Statistical Theory and Modeling for Turbulent Flows", Wiley, 2001.
- B-2) Pope, S.B., "Turbulent Flows", Cambridge University Press, 2000.
- B-3) Nagano etc., "Assessment of  $\epsilon$  -Equations for Wall Shear flows with DNS Database (2nd Report, The case of Second-Order Closure Modeling)", Trans. Jpn. Soc. Mech. Eng., Ser.B, 59-564, (1993-8), 2455.
- B-4) Launder, B.E., Reece, G.J., Rodi, W., "Progress in the Development of a Reynolds-Stress Turbulence Closure.", J. Fluid Mech., 68(3):537–566, April 1975.
- B-5) Hirai etc., "Prediction of the Laminarization Phenomena in Turbulent Swirling Flows", Trans. Jpn. Soc. Mech. Eng., Ser.B, 52-476 (1986-4), 1608.
- B-6) Shima, "A Reynolds Stress Model Incorporating the Effect of Anisotropy (1st Report, Modeling and Application to a Flat Plate Boundary Layer", Trans. Jpn. Soc. Mech. Eng., Ser.B, 54-505 (1988-9), 2317.

## Appendix-C

### Selection of Cavitation Model

#### C-1 Model Description

FLUENT 12.0 provides three models for calculating the cavitation mass transfer rate, i.e., the Singhal model, Zwart-Gerber-Belamri model and Schnerr and Sauer model.

The Singhal model has been derived from the homogenous flow approach. This model solves the vapor mass fraction transport equation,

$$\frac{\partial}{\partial t}(\rho \cdot f_v) + \nabla \cdot (\rho \cdot \vec{V} \cdot f_v) = \nabla \cdot (\Gamma \nabla f_v) + R_e - R_c \quad \text{Eq. C1}$$

This model also assumes that bubble dynamics are described by the generalized Rayleigh-Plesset equation,

$$R_B \frac{D^2 R_B}{Dt^2} + \frac{3}{2} \left( \frac{DR_B}{Dt} \right)^2 = \left( \frac{P_B - P}{\rho_l} \right) - \frac{4v_l}{R_B} \dot{R}_B - \frac{2S}{\rho_l R_B} \quad \text{Eq. C2}$$

The average vapor bubble size is estimated by using

$$R_B = \frac{0.061 \cdot We \cdot \sigma^2}{2\rho_l v_{rel}^2} \quad \text{Eq. C3}$$

Rates of mass exchange are given as a function of bubble diameter and the difference between the bubble pressure and the local far-field pressure,

$$R_e = F_{vap\_SH} \frac{\max(1.0, \sqrt{k})}{\sigma} (1 - f_v - f_g) \rho_l \rho_v \sqrt{\frac{2(P_v - P)}{\rho_l}} \quad \text{Eq. C4}$$

$$R_c = F_{cond\_SH} \frac{\max(1.0, \sqrt{k})}{\sigma} f_v \rho_l \rho_v \sqrt{\frac{2(P - P_v)}{\rho_l}}$$

The Singhal model considers the effect of turbulence on phase change threshold pressure by correcting the vapor saturation pressure,

$$P_v = P_{sat} + \frac{1}{2} (0.39 \times \rho k) \quad \text{Eq. C5}$$

The Zwart-Gerber-Belamri model solves the vapor mass conservation equation with additional mass transfer source terms, which are related to the growth or collapse of the vapor bubbles,

$$\frac{\partial}{\partial t}(\alpha \cdot \rho_v) + \nabla \cdot (\alpha \cdot \rho_v \cdot \vec{V}_v) = R_e - R_c \quad \text{Eq. C6}$$

In this model, the mass transfer source term is calculated by using the bubble number density ( $n$ ) multiplied by the mass change rate of a single bubble. The bubble number density will decrease as the vapor volume fraction increases. The mass transfer source terms in Zwart-Gerber-Belamri model are given as,

$$R_e = F_{vap\_ZGB} \frac{3\alpha_{nuc}(1-\alpha_v)}{R_B} \rho_v \sqrt{\frac{2}{3} \frac{(P_v - P)}{\rho_l}} \quad \text{Eq. C7}$$

$$R_c = F_{cond\_ZGB} \frac{3\alpha_v \rho_v}{R_B} \sqrt{\frac{2}{3} \frac{(P - P_v)}{\rho_l}}$$

The Schnerr and Sauer model follows a similar approach as that of the Singhal model to derive the expression for the net mass transfer from liquid phase to vapor phase. This model solves the vapor mass conservation equation as the following,

$$\frac{\partial}{\partial t}(\alpha \cdot \rho_v) + \nabla \cdot (\alpha \cdot \rho_v \cdot \vec{V}_v) = R = \frac{\rho_v \rho_l}{\rho} \frac{D\alpha}{Dt} \quad \text{Eq. C8}$$

The vapor volume fraction is calculated from the number of bubbles per unit volume of liquid,

$$\alpha = \frac{n_b \frac{4}{3} \pi R_B^3}{1 + n_b \frac{4}{3} \pi R_B^3} \quad \text{Eq. C9}$$

Similar to the Singhal model, the Schnerr and Sauer model also assumes that bubble dynamics are described by the generalized Rayleigh-Plesset equation. Eventually, the mass transfer source terms are given as,

$$R_e = \frac{\rho_v \rho_l}{\rho} \alpha (1 - \alpha) \frac{3}{R_B} \sqrt{\frac{2}{3} \frac{P_v - P}{\rho_l}} \quad \text{Eq. C10}$$

$$R_c = \frac{\rho_v \rho_l}{\rho} \alpha (1 - \alpha) \frac{3}{R_B} \sqrt{\frac{2}{3} \frac{P - P_v}{\rho_l}}$$

The cavitation model capabilities and application limitations in FLUENT 12.0 have been summarized in Table C-1 (Ref. 3)). It can be concluded from this table that any of the three cavitation models could be applied to the advanced accumulator simulation, with compatible multiphase model and turbulence model enabled in the simulation case file.

**Table C-1 Capabilities and Limitations of Three Cavitation Models in FLUENT 12.0**

	<b>Singhal Model</b>	<b>Z-G-B Model*</b>	<b>S&amp;S Model*</b>
Noncondensable Gas Effect	Considered	Not considered	Not considered
Turbulence Model Compatibility	Not compatible with the LES turbulence model	All available turbulence models in FLUENT	All available turbulence models in FLUENT
Multiphase Model Compatibility	Mixture Model	Mixture Model Eulerian Model	Mixture Model Eulerian Model
Solver Compatibility	Pressure-based solver	Pressure-based solver	Pressure-based solver
Liquid/Vapor Phase Compressibility	Incompressible or Compressible	Incompressible or Compressible	Incompressible or Compressible

\* Z-G-B Model: Zwart-Gerber-Belamri model; S&S Model: Schnerr and Sauer model

## C-2 Sensitivity Study of Cavitation Model

### 1. Selection of Cavitation Model

Table C-1 indicates that five possible combinations of cavitation model with multiphase flow model can be chosen to simulate cavitation flows, i.e.,

- (1) Singhal model with Mixture model
- (2) Zwart-Gerber-Belamri model with mixture model
- (3) Schnerr-Sauer model with mixture model
- (4) Zwart-Gerber-Belamri model with Eulerian model
- (5) Schnerr-Sauer model with Eulerian model

All five possible combinations have been tested for simulating the ACC flow under both the small injection rate and the large injection rate conditions. The simulation results show that:

- (i) Simulation cannot reach converged results when Eulerian model is enabled (Options 4 and 5). The Eulerian model is the most sophisticated model among three multiphase models that are provided by FLUENT 12.0. The Eulerian model allows for the modeling of multiple separate, yet interacting phases. Conservation equations of mass, momentum and energy for each phase, and several interfacial momentum and thermal energy exchange constitutive equations are solved in the

Eulerian model. Although this more complex model options increase prediction precision, the Eulerian model exhibits more computational sensitivity which can result in numerical instability during the solution process. It has been observed that a coarser mesh or other model simplifications are required in order to achieve converged solutions, which reduced the overall accuracy of the simulation results.

When Mixture model is applied, the Chimera meshing option was enabled in order to achieve desired  $Y^+$  value near the wall (refer to 3.2.2). The simulation results show that:

- (ii) Simulations with Schnerr-Sauer model cannot reach converged results (Option 3). In these calculation processes, the mass flow rates at the inlet and the outlet are imbalanced and the calculation terminates before convergence is achieved.
- (iii) Simulation with Singhal model does not have the above mentioned problems and results in converged mass-balanced solutions.

Thus, the Singhal model combined with the Mixture multiphase model has been chosen in this CFD study for ACC under both the small flow injection and the large flow injection conditions.

Furthermore, it is generally known that cavitation may occur at static pressures larger than saturation pressure due to the effect of turbulence (see, for example, Reference 19). Although three cavitation models are available in FLUENT 12.0, only the Singhal model can model the effect of turbulence on cavitation inception. Thus, the Singhal model is superior to the other models for modeling cavitation inception in the ACC analyses. To provide additional confirmation of whether it is appropriate to apply the Singhal model, CFD calculations have been performed in order to evaluate the sensitivity for calculating scale effects using an alternate cavitation model in FLUENT 12.0.

In Appendix-I, the sensitivity calculations include a sensitivity case where the outlet boundary pressure is reduced to the atmospheric pressure. Even in this case, the flow rate coefficient is not changed although a larger amount of cavitation void occurs in the center of the vortex chamber and outlet nozzle, compared with the other cases. The same result was obtained for the both 1/2 and 1/1 scale model. Therefore, it is concluded that the small flow rate is insensitive to the cavitation void without scaling concerns. Therefore the sensitivity analysis of cavitation model is performed for large flow injection.

## 2. Calculation conditions

For large flow, Case 3-5 sec was analyzed for the sensitivity calculations, since cavitation is most likely to occur for this case. The “Fine” mesh with the Chimera mesh refinement has been utilized in these calculations in order to provide adequate  $Y^+$  value (approximately 300, as recommended by the FLUENT users manual). Therefore, the friction and velocity gradients at the wall are modeled with sufficient accuracy.

In the calculation with fine mesh, the calculations for the ZGB and SS models using RSM and 2<sup>nd</sup>-order do not achieve convergence. In these calculation processes, the mass flow rates at the inlet and the outlet are imbalanced and the calculation terminates before

convergence is achieved. For large flow, the anisotropic turbulence modeling used in the RSM model is considered to be less important than wall modeling and cavitation inception. Therefore, the 1<sup>st</sup>-order k-omega turbulence model is used to obtain stable solutions. However the calculations for the SS model do not converge. So the sensitivity for calculating scale effects models is evaluated in Singhal model and ZGB model. In FLUET 12.0 Documentation, it can be confirmed that the solution of SS and ZGB models are good agreement in the validation calculation of orifice cavitation (Chapter 15. Figure 15.4.1, Page 15-4 in Reference 3). Thus the evaluation of the sensitivity for calculating scale effects without SS models is considered acceptable. The adequacy of using 1<sup>st</sup>-order k-omega instead of 2<sup>nd</sup>-RSM for turbulence model is discussed further below.

### 3. Results of calculations

**Table C-2 Calculation Conditions for Singhal and ZGB Models**

**Table C-3 Scale Effects in Snghal an ZGB Models for Large Flow**





**Figure C-1 Void Fraction Distribution at the Throat (Case 3 Large Flow 5 sec, Fine Mesh)**

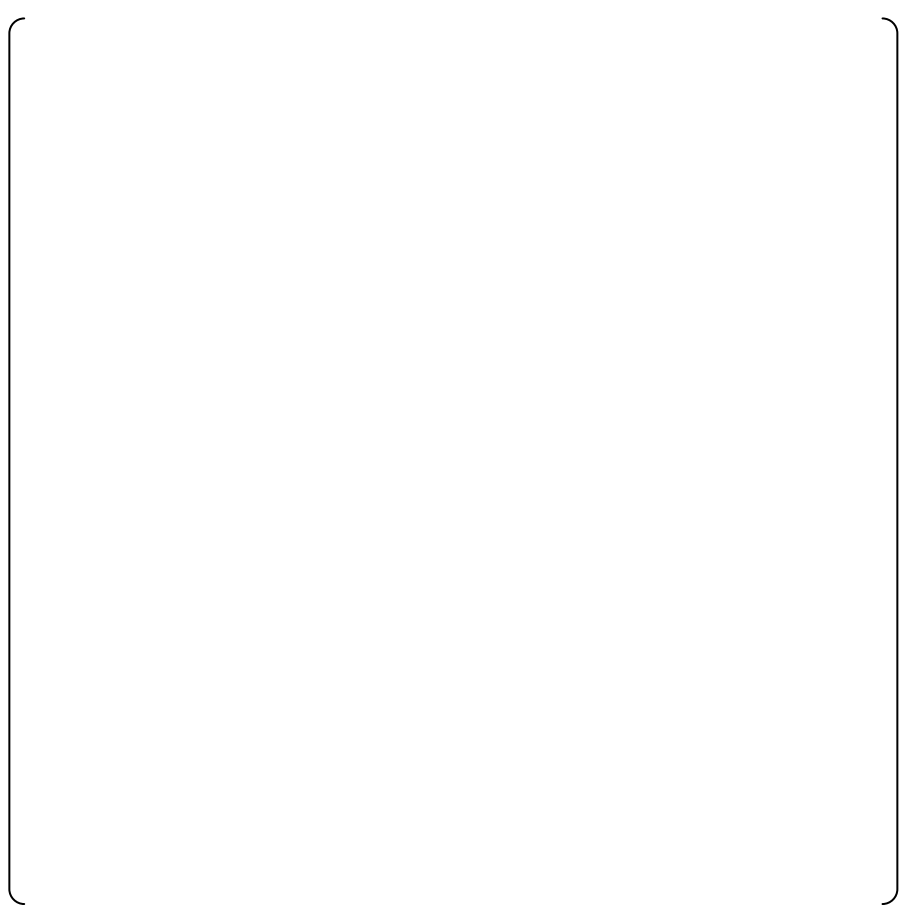


**Figure C-2 Total Pressure Loss of Vortex Chamber, Reducer and Diffuser**

### C-3 Justification of Singhal Model

#### Applicability of Singhal Model

The model author has made the following assumptions when deriving the Singhal model,

- (i). Assuming homogenous two-phase flow (Equal-Velocity-Equal-Temperature)
- (ii). Assuming that flow is isothermal with constant fluid properties
- (iii). Assuming that noncondensable gas mass fraction is constant in the flow field
- (iv). Utilizing the generalized Rayleigh-Plesset equation to describe the bubble growth process, while ignoring the viscous damping term and surface tension term
- (v). Ignoring the second-order derivative of  $R_B$
- (vi). Estimating bubble diameter based on Eq. C3
- (vii). Assuming that the phase change rate is proportional to the slip velocity between the vapor phase and liquid phase, instead of proportional to the square of slip velocity
- (viii). Assuming that characteristic velocity can be expressed as the square root of local turbulent kinetic energy  $\sqrt{k}$
- (ix). Treating the effect of turbulence on cavitation phase-change threshold pressure by using Eq. C5

All these assumptions are acceptable for the ACC flow field based on the following reasons:

- (i). Cavitation occurs at the downstream of nozzle throat in the outlet injection pipe. At that position, liquid flow velocity is expected to be much larger than the slip velocity between vapor bubbles and liquid.
- (ii). The ACC injection process can be treated as isothermal.

Thus, the Singhal model can be applied to the ACC simulations.

#### Scaling Effect of Singhal Model

The Singhal model solves vapor mass conservation equation (Eq. C1), with the mass transfer rate terms as given in Eq. C4. These equations can be converted to dimensionless format if the following parameters are defined,

$$t^* = \frac{t}{t_0}, \quad \rho_v^* = \frac{\rho_v}{\rho_{v,0}}, \quad x^* = \frac{x}{L_0}, \quad u^* = \frac{u}{u_0}, \quad C_e^* = \frac{C_e}{C_{e,0}}, \quad \text{Eq. C11}$$

$$k^* = \frac{k}{k_0}, \quad \sigma^* = \frac{\sigma}{\sigma_0}, \quad \rho_l^* = \frac{\rho_l}{\rho_{l,0}}, \quad P^* = \frac{P}{\rho_{l,0} u_0^2}$$

Here, subscript 0 refers to an appropriate reference value.

Equation C1 can be re-written as,

$$\frac{\rho_{v,0}}{t_0} \frac{\partial}{\partial t^*} (\alpha \cdot \rho_v^*) + \frac{\rho_{v,0} \cdot u_0}{L_0} \nabla^* \cdot (\alpha \cdot \rho_v^* \cdot \vec{V}_v^*) = \frac{C_{e,0} \cdot \sqrt{k_0} \cdot \rho_{l,0} \cdot \rho_{v,0} \cdot u_0}{\sigma_0} (R_e^* - R_c^*) \quad \text{Eq. C12}$$

which can be re-arranged as,

$$\frac{\partial}{\partial t^*} (\alpha \cdot \rho_v^*) + \frac{t_0 \cdot u_0}{L_0} \nabla^* \cdot (\alpha \cdot \rho_v^* \cdot \vec{V}_v^*) = \frac{C_{e,0} \cdot \sqrt{k_0} \cdot \rho_{l,0} \cdot u_0 \cdot t_0}{\sigma_0} (R_e^* - R_c^*) \quad \text{Eq. C13}$$

Two dimensionless numbers appear in (Eq. 13), such as,

$$\Pi_1 = \frac{t_0 \cdot u_0}{L_0} \quad \text{Eq. C14}$$

$$\Pi_2 = \frac{C_{e,0} \cdot \sqrt{k_0} \cdot \rho_{l,0} \cdot u_0 \cdot t_0}{\sigma_0} = \frac{\rho_{l,0} \cdot u_0^2 \cdot L_0}{\sigma_0}$$

$\Pi_1$  represents the ratio of transient time to the flow characteristic time.  $\Pi_2$  is similar to the Weber number, represents the ratio of inertia to surface tension force. Considering the physical meaning of dimensionless group  $\Pi_2$ , an appropriate reference value for length scale,  $L_0$ , is the bubble diameter. Eq. C13 will generate same cavitation solutions for ACC systems with different length scale, under the situation that values of  $\Pi_1$  and  $\Pi_2$  are same, and same initial condition and boundary conditions have been imposed for these ACC systems.

It is expected that typical bubbles generated in the cavitation process will be very small, i.e., their diameters will be less than a few millimeters, and the two-phase flow structure is expected to be bubbly flow. The following equation can be utilized to estimate the average bubble diameter for bubbly flow,

$$D_b = 2 \sqrt{\frac{\sigma}{g \cdot \Delta \rho}} \quad \text{Eq. C15}$$

From the advanced accumulator working conditions, the average bubble diameter can be estimated to be [     ] mm from the above equation. This means that the throat size of 1/2 scale ACC is much larger than a typical bubble size. Thus, the Singhal model describes a local phenomena, which is related to the length scale of a vapor bubble. Therefore, the performance of the Singhal model will be the same for 1/2 scale ACC simulations and for 1/1 scale ACC simulations.

### Applicability of Singhal Model to High Void Fraction Regions

Two assumptions for deriving the Singhal model are related to the low void fraction flow conditions, such as, the flow is homogenous and the generalized Rayleigh-Plesset equation can be utilized to describe the bubble growing process. However, the model also contains two empirical constants,  $C_e$  and  $C_c$ , to adjust the vapor generation/condensation rates.

$$R_e = C_e \frac{V_{ch}}{\sigma} (1-f) \rho_l \rho_v \sqrt{\frac{2}{3} \frac{(P_v - P)}{\rho_l}} \quad \text{Eq. C16}$$

$$R_c = C_c \frac{V_{ch}}{\sigma} f \rho_l \rho_v \sqrt{\frac{2}{3} \frac{(P - P_v)}{\rho_l}} \quad \text{Eq. C17}$$

These empirical constants have been decided by comparing the CFD results with various cavitation flows, including sharp-edged orifice flows and hydrofoil flows. The following validation calculations conducted by several researchers show that the Singhal model can give reasonable predictions for pressure variation and cavitation number for high-speed flow cavitation on hydrofoils and submerged cylindrical bodies. These validation calculation results contain high void fraction (up to 1.0) regions near the wall, which demonstrates that the Singhal model can be applied to high void fraction occurred in a small region and achieve good agreement with experimental results.

Watanabe et. al.(Ref.9) performed RANS simulations of flow around two different conventional propellers at non-cavitating and cavitating operating conditions by applying the Singhal model. Predicted values of the propeller thrust coefficients and torque coefficients in uniform flow under large angle of attack conditions are in a good agreement with the measured data. The simulation predicts that high vapor void fraction regions occur on the backside of the propeller blade. The predicted cavity shape on the blade is in good agreement with the observed cavity shapes in the experiment (Fig. 16 in Reference 9).

Huang et. al.(Ref.17) utilizes the Singhal model combined with a linear viscous turbulent method to simulate steady cavitation flow over NACA66 2-D hydrofoils. The predicted pressure distribution on the hydrofoil surface fits well with the measured data. High void fraction regions appear near the wall (Fig. 7 and Fig. 8 in Reference 17). General characteristics of the predicted cavity region fit well with experimental observations. For example, the predicted cavity length grows with the increase of the angle of attack, and with the decrease of the cavitation numbers.

Dular et. al.(Ref.18) performed an experimental and numerical study of developed cavitating flow around two hydrofoils. The PIV (Particle Image Velocimetry) and LIF (Laser Induced Fluorescence) techniques were adopted in the experiment to measure the velocity and void ratio fields around the hydrofoils. The Singhal model was applied to predict the vapor generation process. Comparisons between the numerical and experimental results show good agreement, including the distribution and size of vapor structures and velocity

fields. The distribution of pressure on the hydrofoil surface has been correctly predicted using the Singhal model.

## Appendix-D

## Consideration for Boundary Condition in Small Flow Injection

For small flow injection, flow rate boundary conditions are used on the water surfaces in the tank and the standpipe in order to stabilize the calculations. Therefore, the resulting pressure on the water surface obtained by analysis is not constant and has a slight difference from the measured pressure. To determine that this difference is not significant, an analysis was performed, for which the water surface at small flow inlet is specified as a pressure boundary condition. This pressure boundary condition result is consistent with the flow rate boundary condition result. (Note that the water surface in the standpipe is specified as a flow rate boundary condition for both analyses.) Table D-1 shows the calculation conditions used in CFD, and Table D-2 shows the calculation results. Flow rate coefficients and flow structures of both the flow rate boundary condition and pressure boundary condition are consistent. Thus, difference in the applied boundary condition (flow rate or pressure) is negligible and the validity for using the flow rate boundary condition is confirmed.

### Table D-1 Calculation Conditions of CFD

### Table D-2 Calculation Results of CFD



**(a) Void Fraction**



**(b) Velocity Contour**



**(c) Static Pressure**

**Figure D-1 Comparison of Inlet Boundary Conditions for Small Flow Injection**



**Appendix-E****Flow Structure for Large Flow**

The body of this report includes flow structure plots of static pressure, velocity vector, and void fraction for the limiting CFD cases of interest. This appendix includes flow structure plots for the remaining CFD cases analyzed, for the large flow condition.

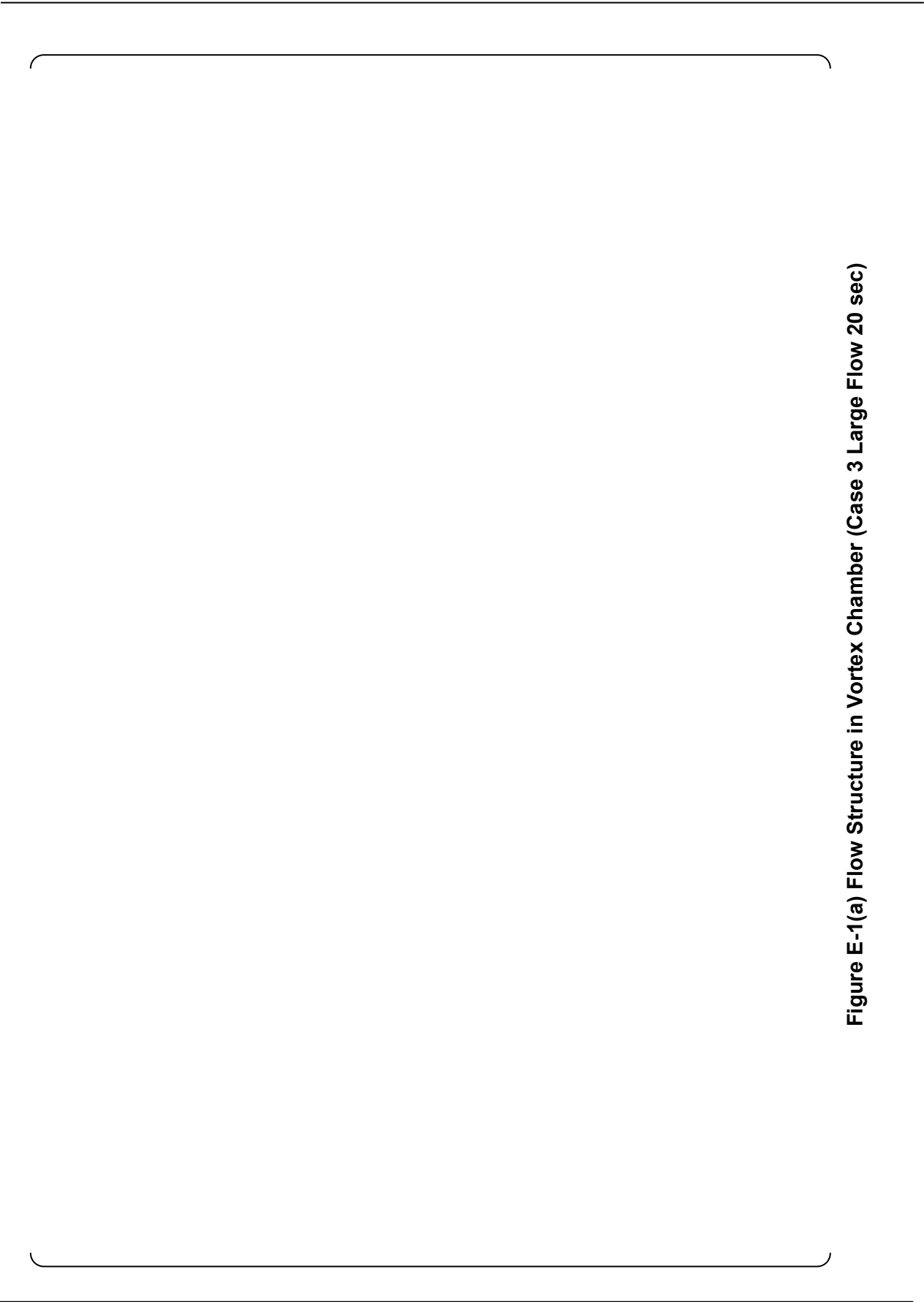


Figure E-1(a) Flow Structure in Vortex Chamber (Case 3 Large Flow 20 sec)

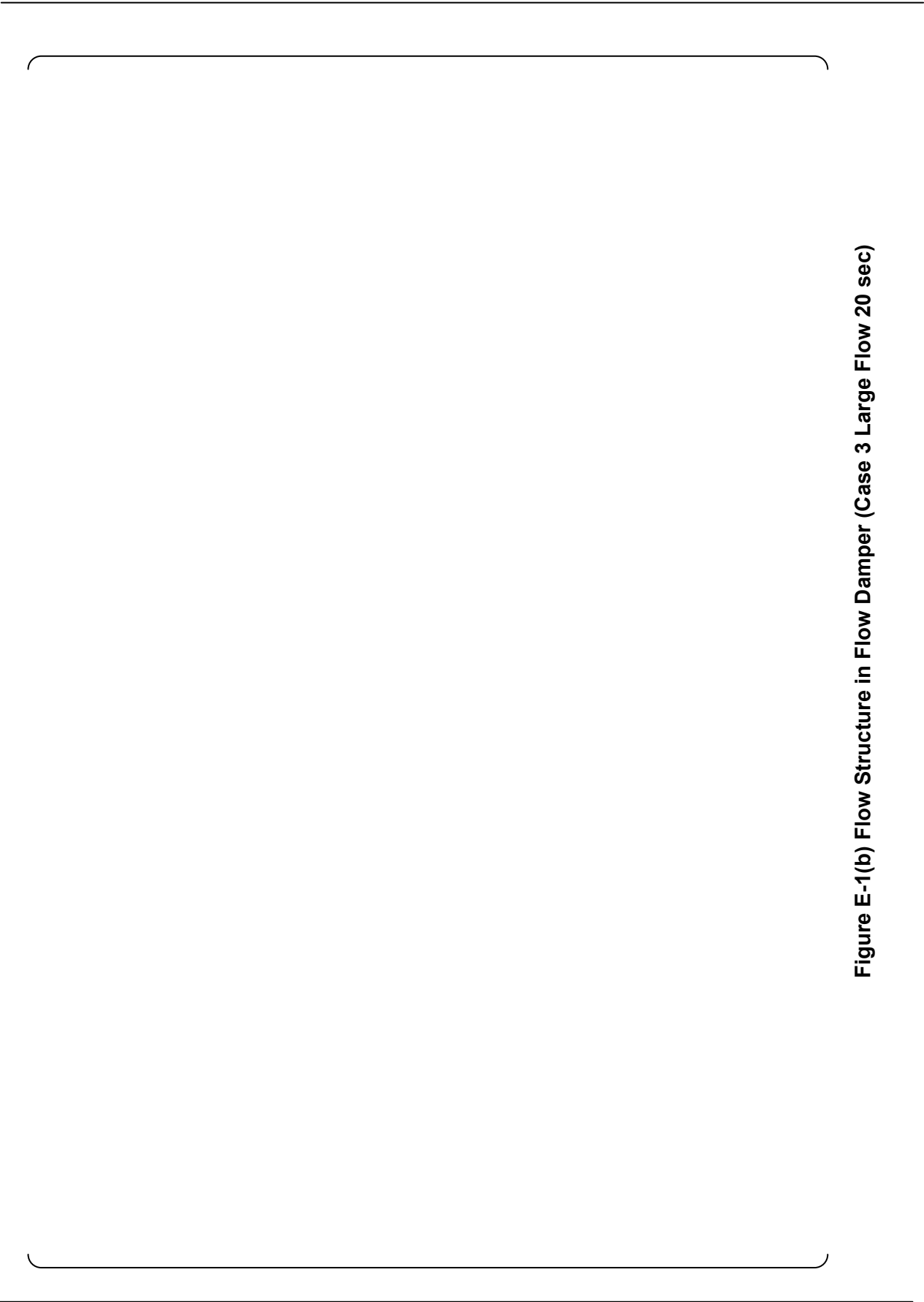


Figure E-1(b) Flow Structure in Flow Damper (Case 3 Large Flow 20 sec)

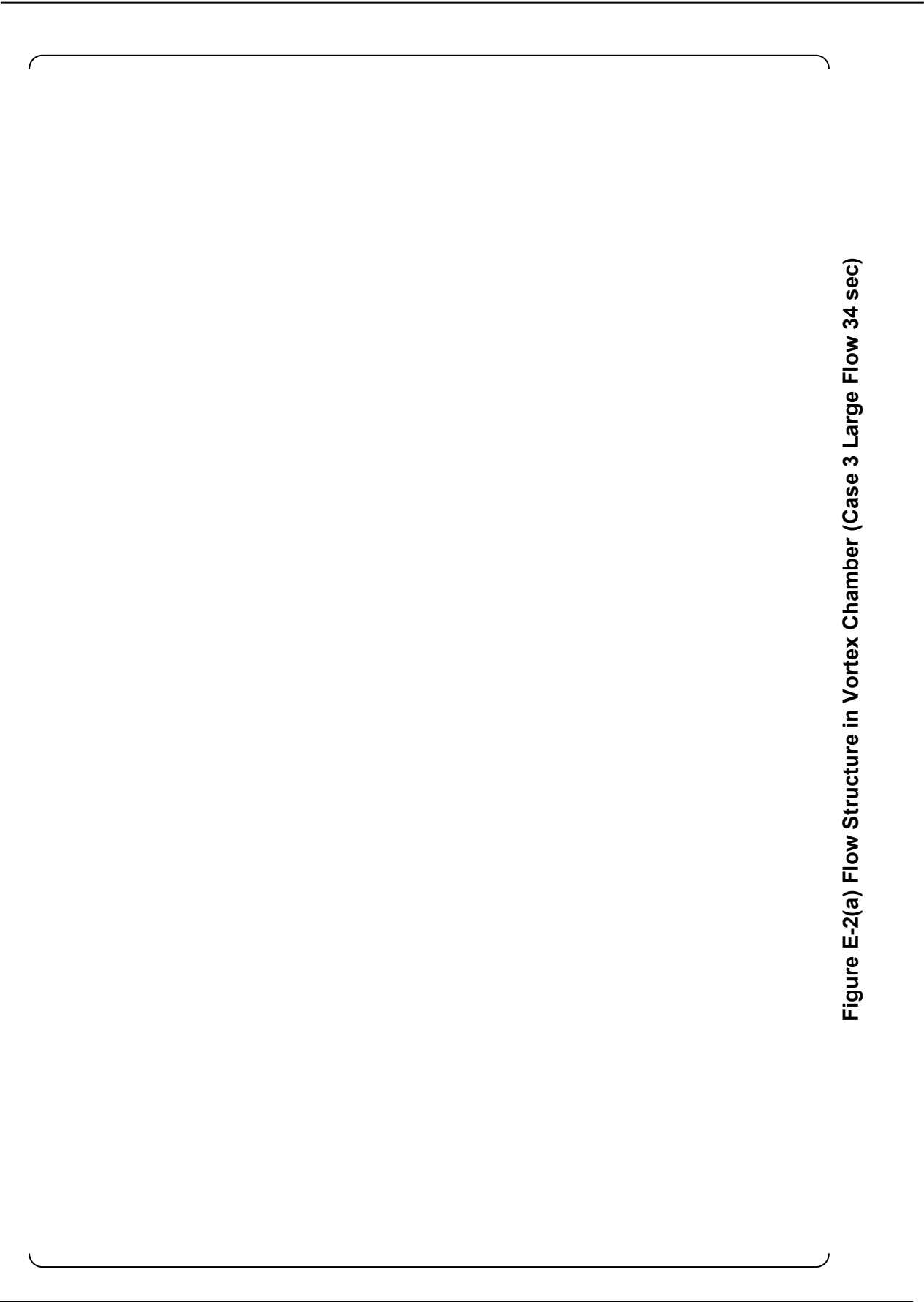


Figure E-2(a) Flow Structure in Vortex Chamber (Case 3 Large Flow 34 sec)

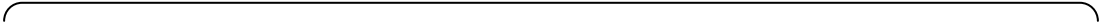


Figure E-2(b) Flow Structure in Flow Damper (Case 3 Large Flow 34 sec)



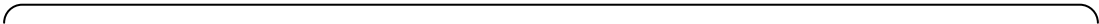


Figure E-3(a) Flow Structure in Vortex Chamber (Case 6 Large Flow 5 sec)



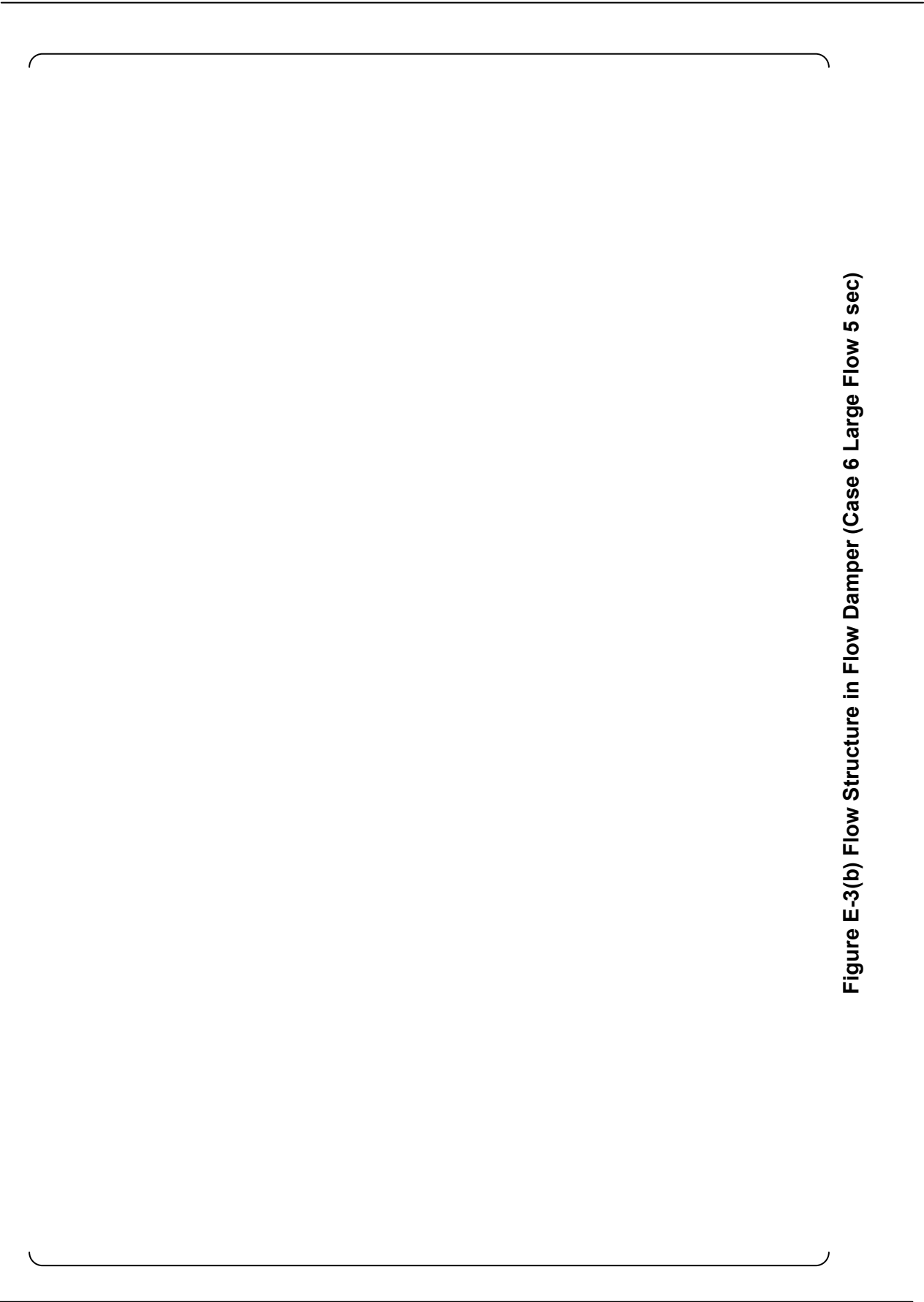


Figure E-3(b) Flow Structure in Flow Damper (Case 6 Large Flow 5 sec)



Figure E-4(a) Flow Structure in Vortex Chamber (Case 6 Large Flow 11 sec)



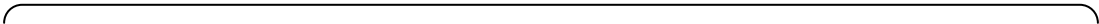


Figure E-4(b) Flow Structure in Vortex Chamber (Case 6 Large Flow 11 sec)



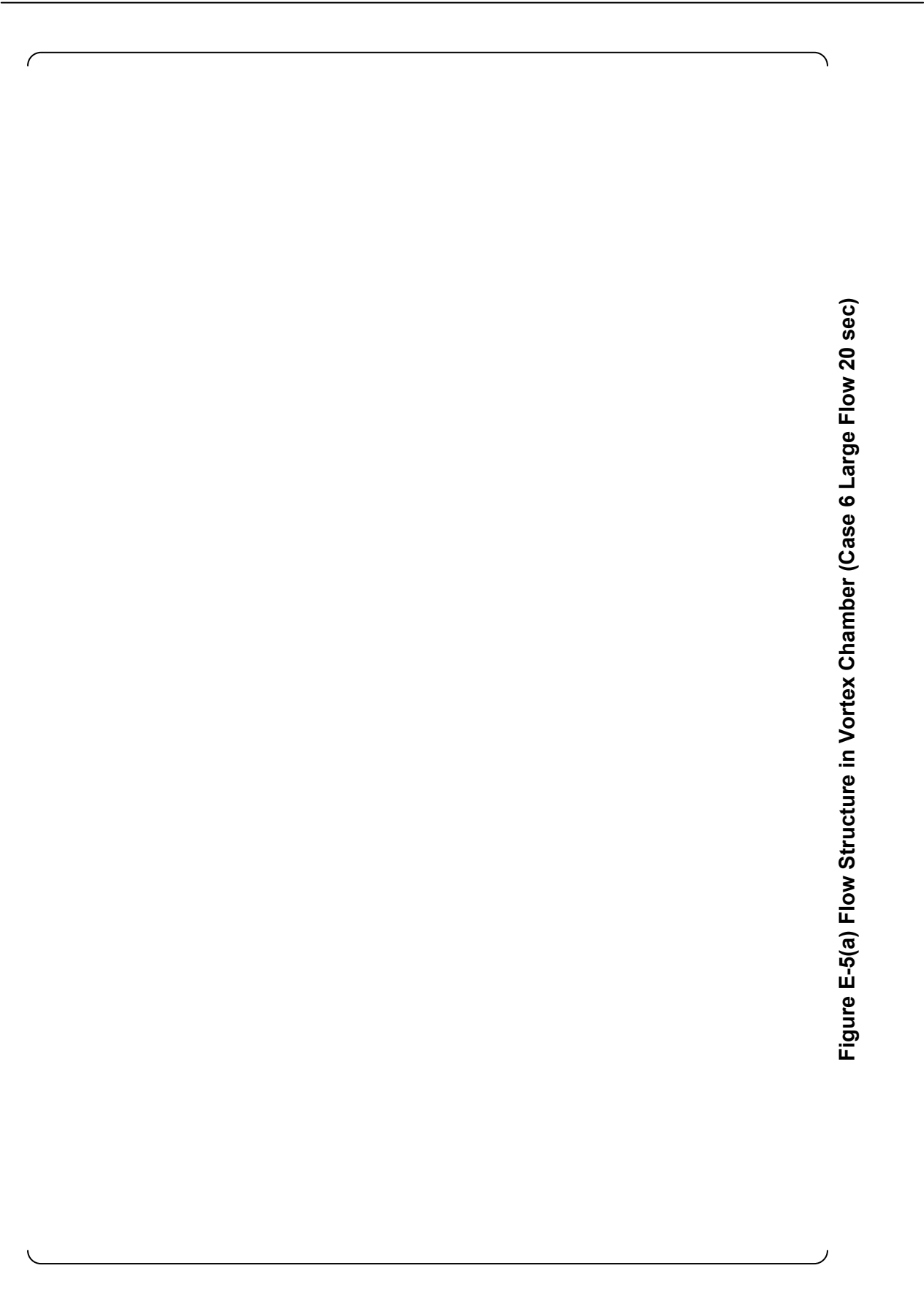
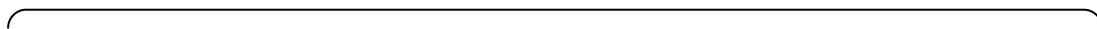


Figure E-5(a) Flow Structure in Vortex Chamber (Case 6 Large Flow 20 sec)



Figure E-5(b) Flow Structure in Flow Damper (Case 6 Large Flow 20 sec)





**Figure E-6(a) Flow Structure in Vortex Chamber (Case 6 Large Flow 50 sec)**



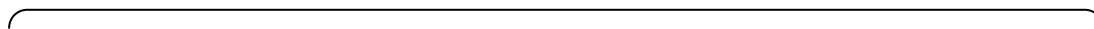


**Figure E-6(b) Flow Structure in Flow Damper (Case 6 Large Flow 50 sec)**



**Appendix-F****Flow Structure for Small Flow**

The body of this report includes flow structure plots of static pressure, velocity vector, void fraction, reverse flow region and location of max. value of deference of absolute pressure and vapor pressure for the limiting CFD cases of interest. This appendix includes flow structure plots for the remaining CFD cases analyzed, for the small flow condition.

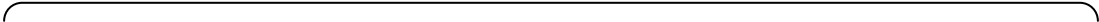


Figure F-1(a) Flow Structure in Vortex Chamber (Case 3 Small Flow 100 sec)





Figure F-1(b) Flow Structure in Flow Damper (Case 3 Small Flow 100 sec)





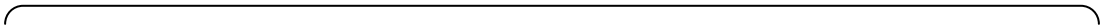


Figure F-2(a) Flow Structure in Vortex Chamber (Case 3 Small Flow 125 sec)



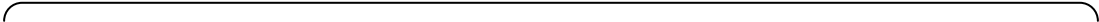


Figure F-2(b) Flow Structure in Flow Damper (Case 3 Small Flow 125 sec)



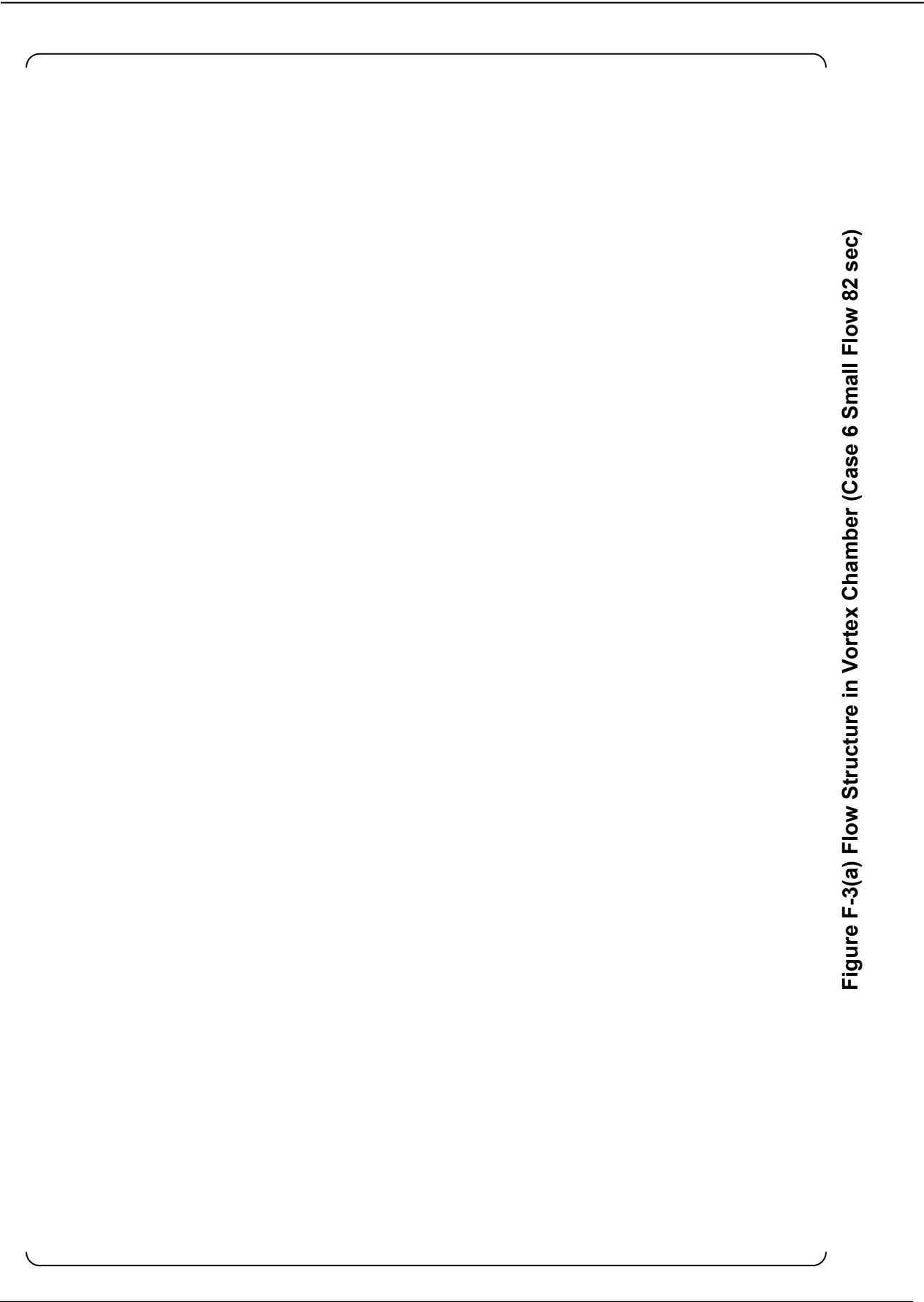


Figure F-3(a) Flow Structure in Vortex Chamber (Case 6 Small Flow 82 sec)



Figure F-3(b) Flow Structure in Flow Damper (Case 6 Small Flow 82 sec)



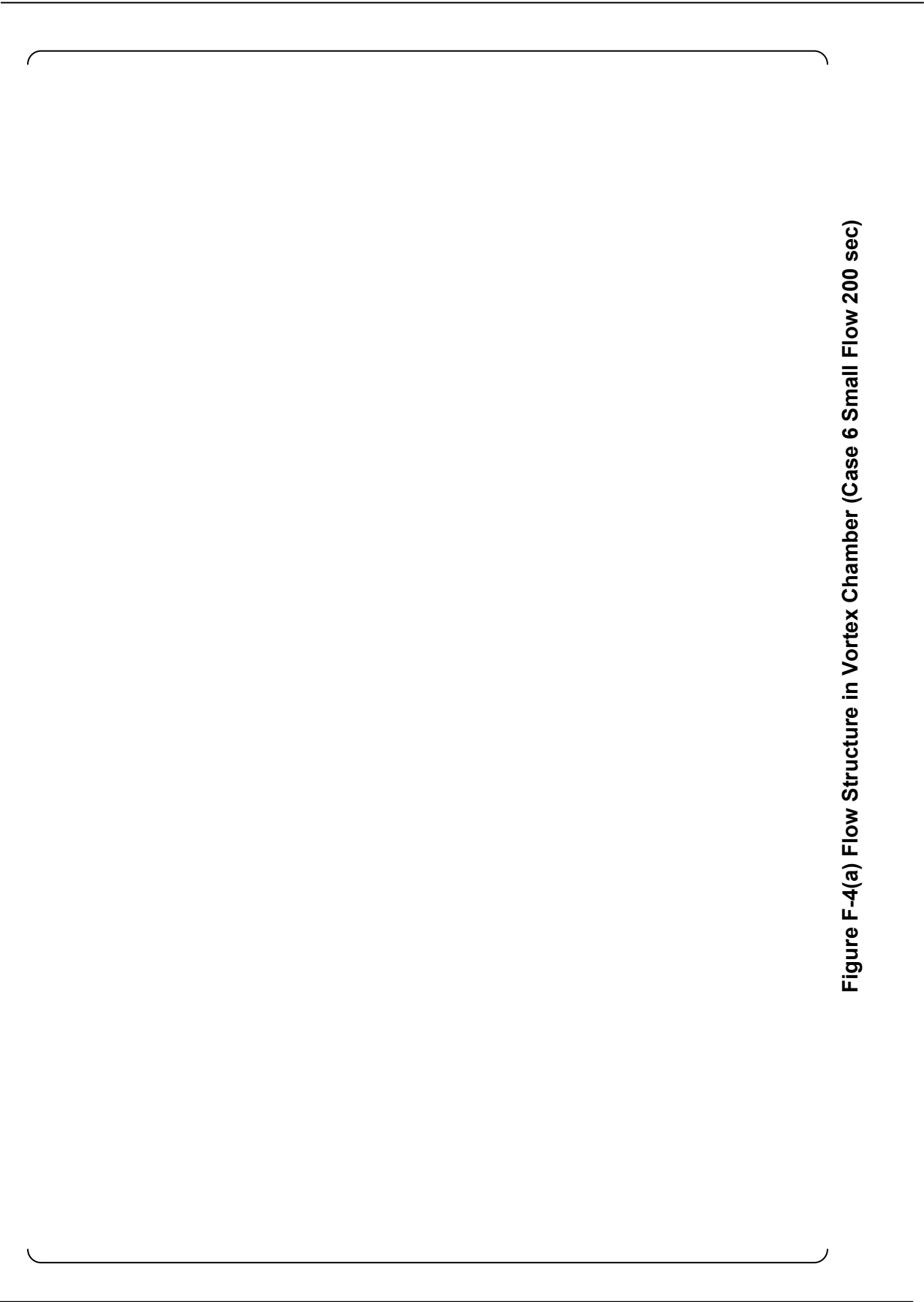


Figure F-4(a) Flow Structure in Vortex Chamber (Case 6 Small Flow 200 sec)

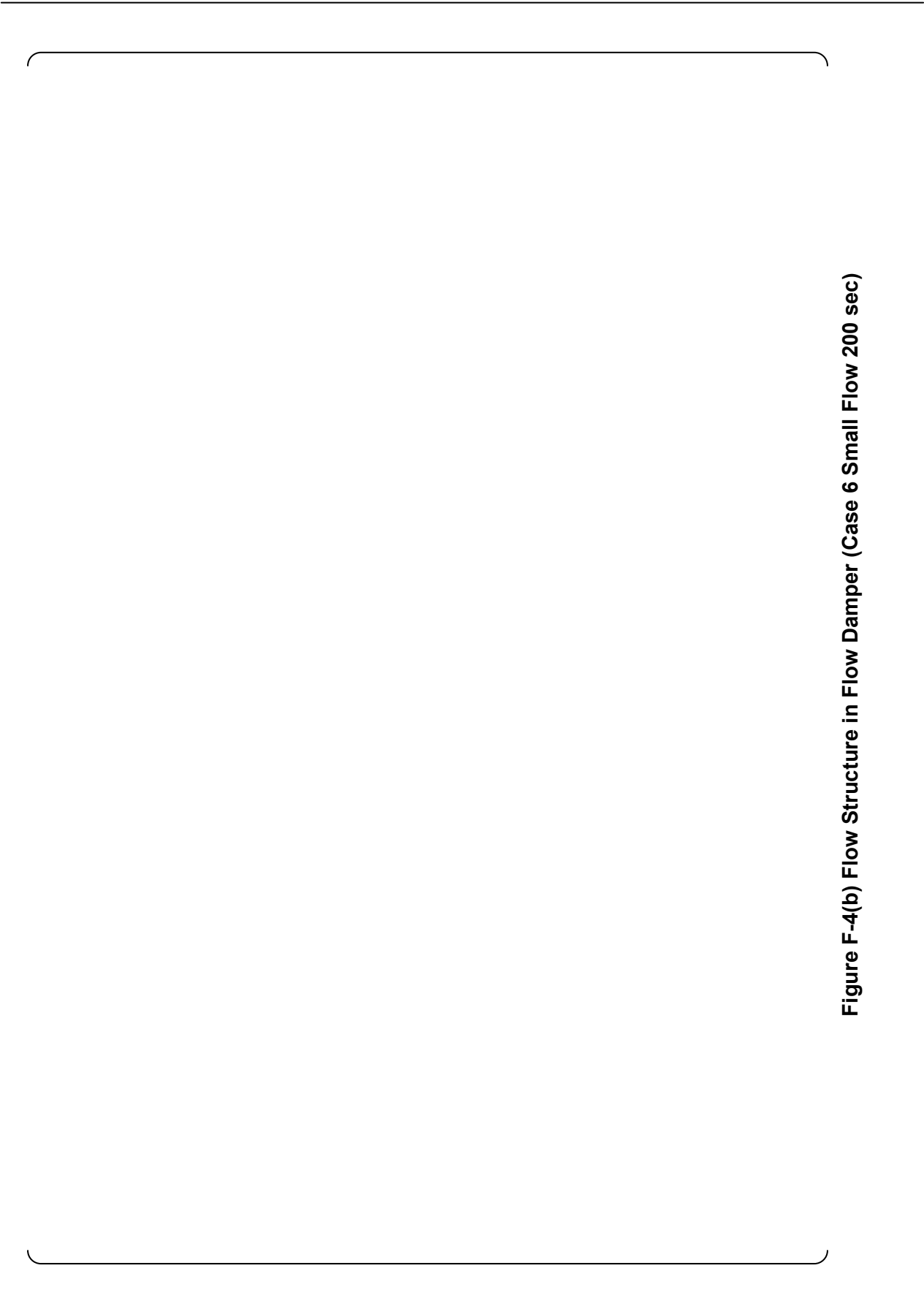
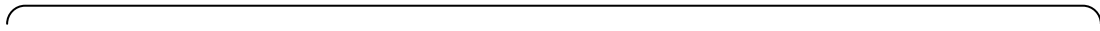


Figure F-4(b) Flow Structure in Flow Damper (Case 6 Small Flow 200 sec)



Figure F-5(a) Flow Structure in Vortex Chamber (Case 6 Small Flow 290 sec)





**Figure F-5(b) Flow Structure in Flow Damper (Case 6 Small Flow 290 sec)**





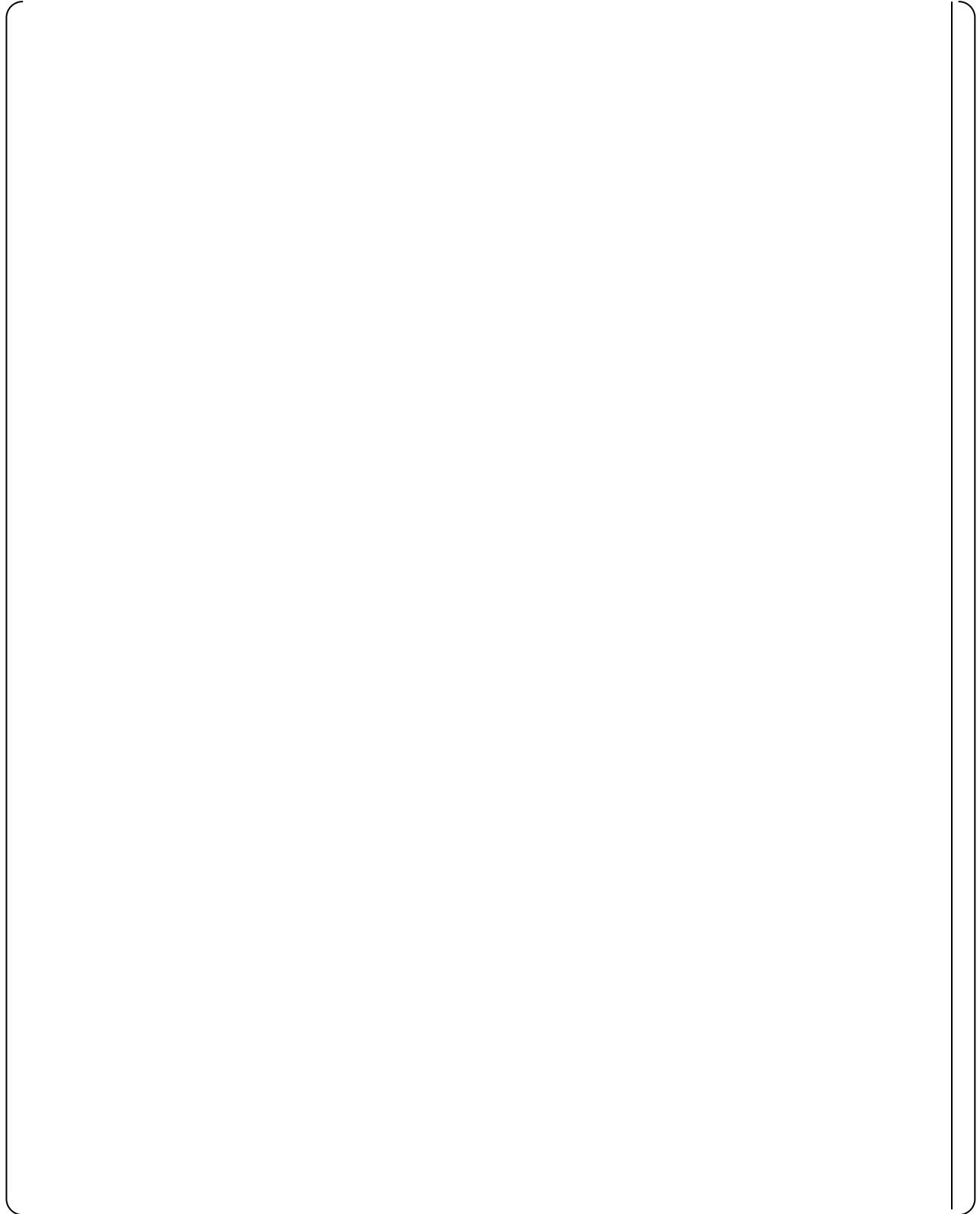


**Figure F-6(a) Reverse Flow Region (1/2 Scale, Case 3 Small Flow)**

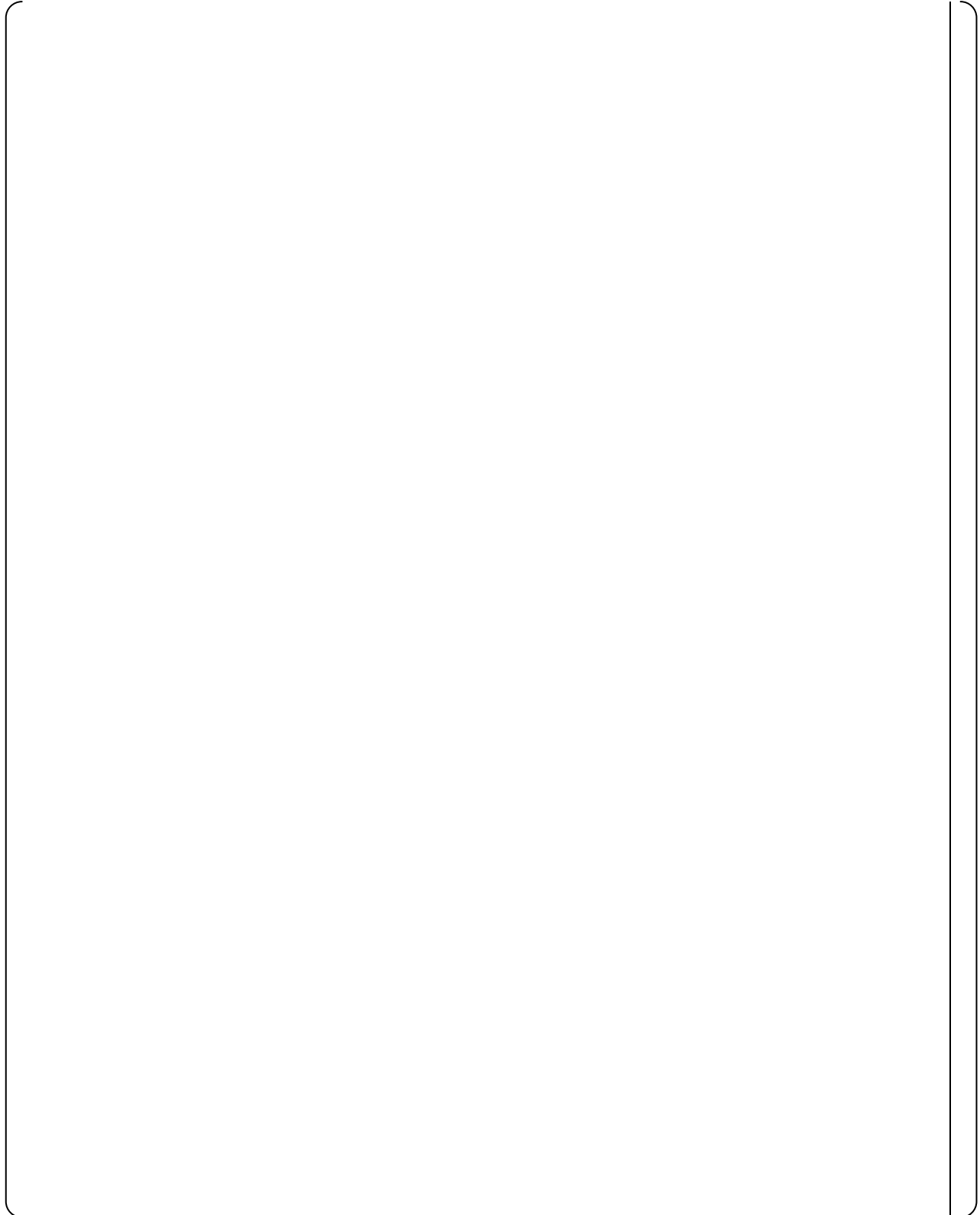


**Figure F-6(b) Reverse Flow Region (1/2 Scale, Case 6 Small Flow)**

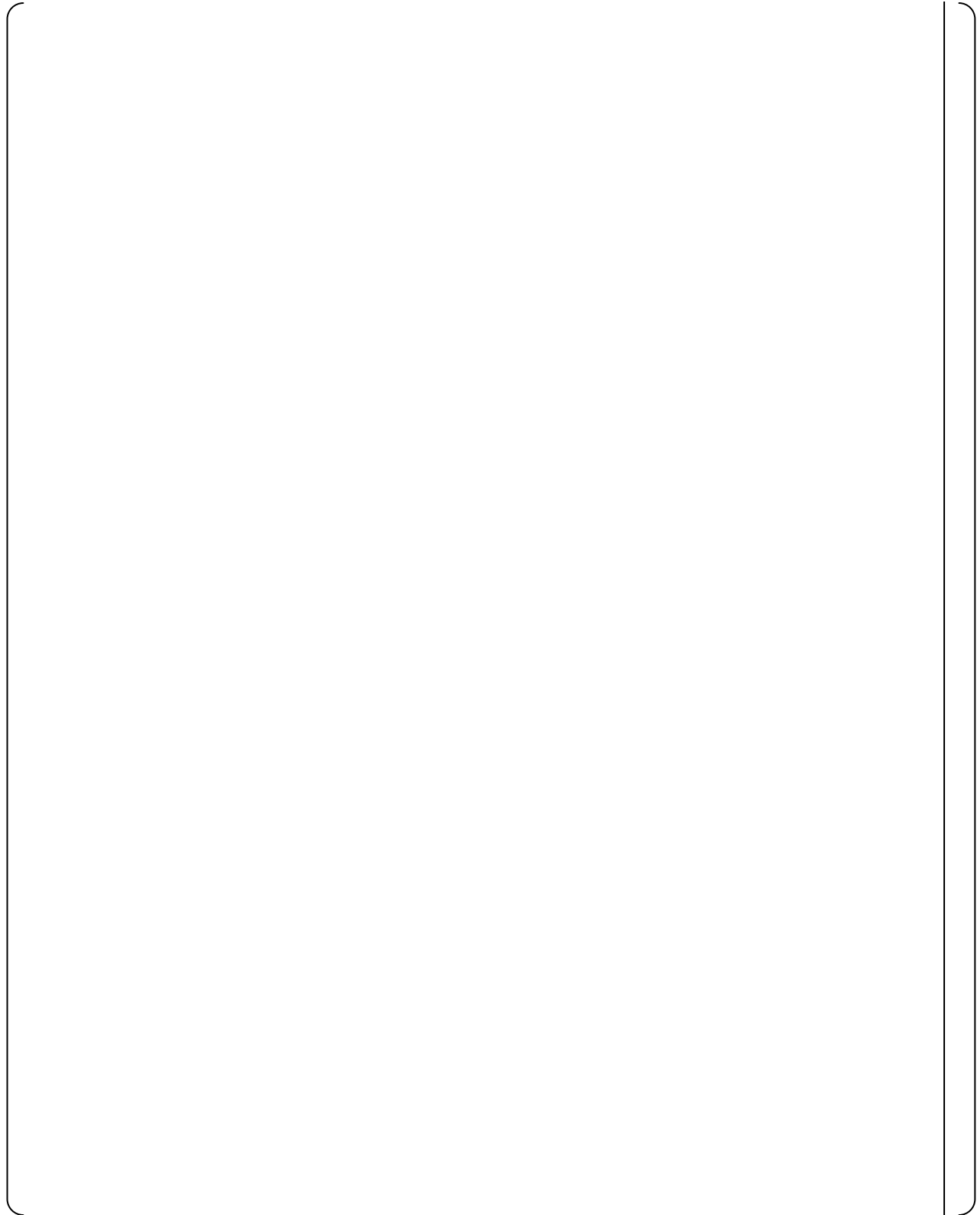


**Figure F-6(c) Reverse Flow Region (1/1 Scale, Case 3 Small Flow)**

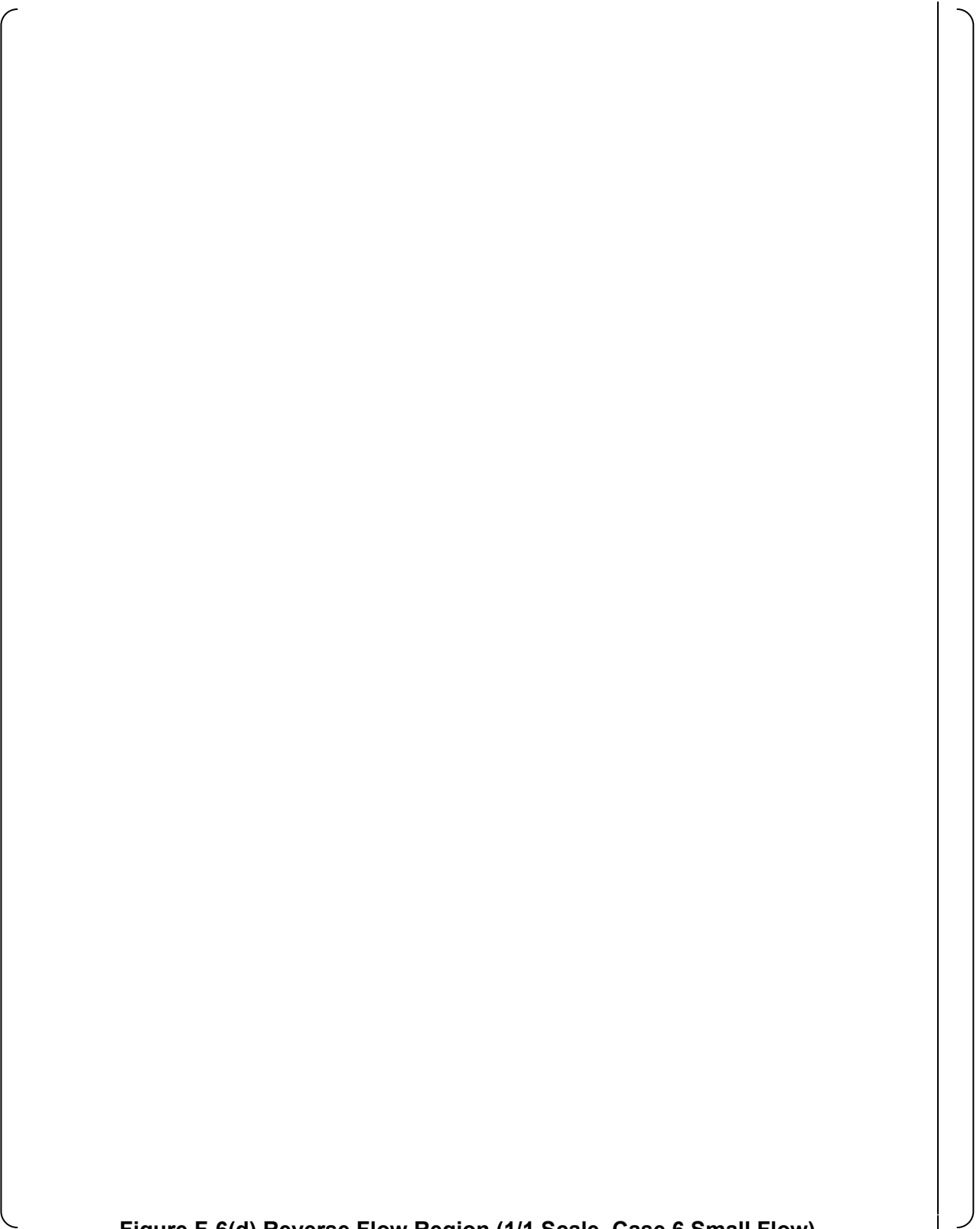


**Figure F-6(d) Reverse Flow Region (1/1 Scale, Case 6 Small Flow)**



**Figure F-7(a) Location of Max. value of Deference between Absolute Pressure and Critical Pressure of Cavitation (1/2 scale, Small Flow)**



**Figure F-7 (b) Location of Max. value of Deference between Absolute Pressure and Critical Pressure of Cavitation (1/1 scale, Small Flow)**

**Appendix-G****Y+ Profile**

Y+ of large flow injection is less than 300 at throat and diffuser where flow resistance is dominated. Thus it is confirmed that the effect of the boundary layer can be adequately evaluated under the current grid (See Figure G-1).

Y+ of small flow injection is less than 100 at the vortex chamber except around the exit where the swirl flow causes large flow resistance. It means that the effect of the boundary layer can be adequately evaluated under the current grid (See Figure G-2).

In small flow injection, Y+ of 1/1 scale model is larger than the value of the 1/2 scale model at the wall of outlet nozzle. This is caused by the difference of the cell thickness near the wall in both models. However the influence on flow resistance is negligible because the shear stresses are almost the same in both scale models (See Figure G-3).



**Figure G-1 Y+ Distribution of Large Flow**



**Figure G-2 Y+ Distribution of Small Flow**



**Figure G-3 Shear Stress Distribution of Small Flow**



## Appendix-H

## Validity Evaluation of Tolerance Interval

The computational method is verified by the numerical value described in ASME PTC 19.1-2005

**Table H-1 Factors for Calculating the Two-Sided 90% and 95% Probability Intervals for a Normal Distribution (Ref.15))**

Number of Given Observations	Factors for Tolerance Interval to Contain at Least 90% and 95% of the Population	
	$C_{T,90}(n)$	$C_{T,95}(n)$
n		
4	5.37	6.37
5	4.28	5.08
6	3.71	4.41
7	3.37	4.01
8	3.14	3.73
9	2.97	3.53
10	2.84	3.38
11	2.74	3.26
12	2.66	3.16
15	2.48	2.95
20	2.31	2.75
25	2.21	2.63
30	2.14	2.55
40	2.05	2.45
60	1.96	2.33
$\infty$	1.64	1.96

$C_{T,90}(n)$  and  $C_{T,95}(n)$  are related as follows as a result of examining the numerical values above.

$$C_{T,90}(n) = C_{T,95}(n)/1.96 \times 1.645$$

$$(\text{Example. } 3.37 = C_{T,90}(7) = C_{T,95}(7)/1.96 \times 1.645 = 4.01/1.96 \times 1.645)$$

1.96 : Corresponds to 95% confidence interval in normal distribution.

1.645 : Corresponds to 90% confidence interval in normal distribution.

$C_{T,90}(n)$  and  $C_{T,95}(n)/1.96 \times 1.645$  are equaled. That is, the technique described in the report is appropriate to derive a 95% confidence interval from a limited sample.

## Appendix-I

### Effect of Cavitation on Small Flow Hydraulic Performance

**Table I-1 CFD Boundary Conditions for Sensitivity Analysis Regarding Cavitation Occurrence**



**Figure I-1(a) Flow Structure in Vortex Chamber (at mid-height)**

Figure I-1(b) Flow Structure in Vortex Chamber and Outlet Nozzle

Figure I-1(c) Critical Pressure of Cavitation and Void Fraction in vortex Chamber and Outlet Nozzle

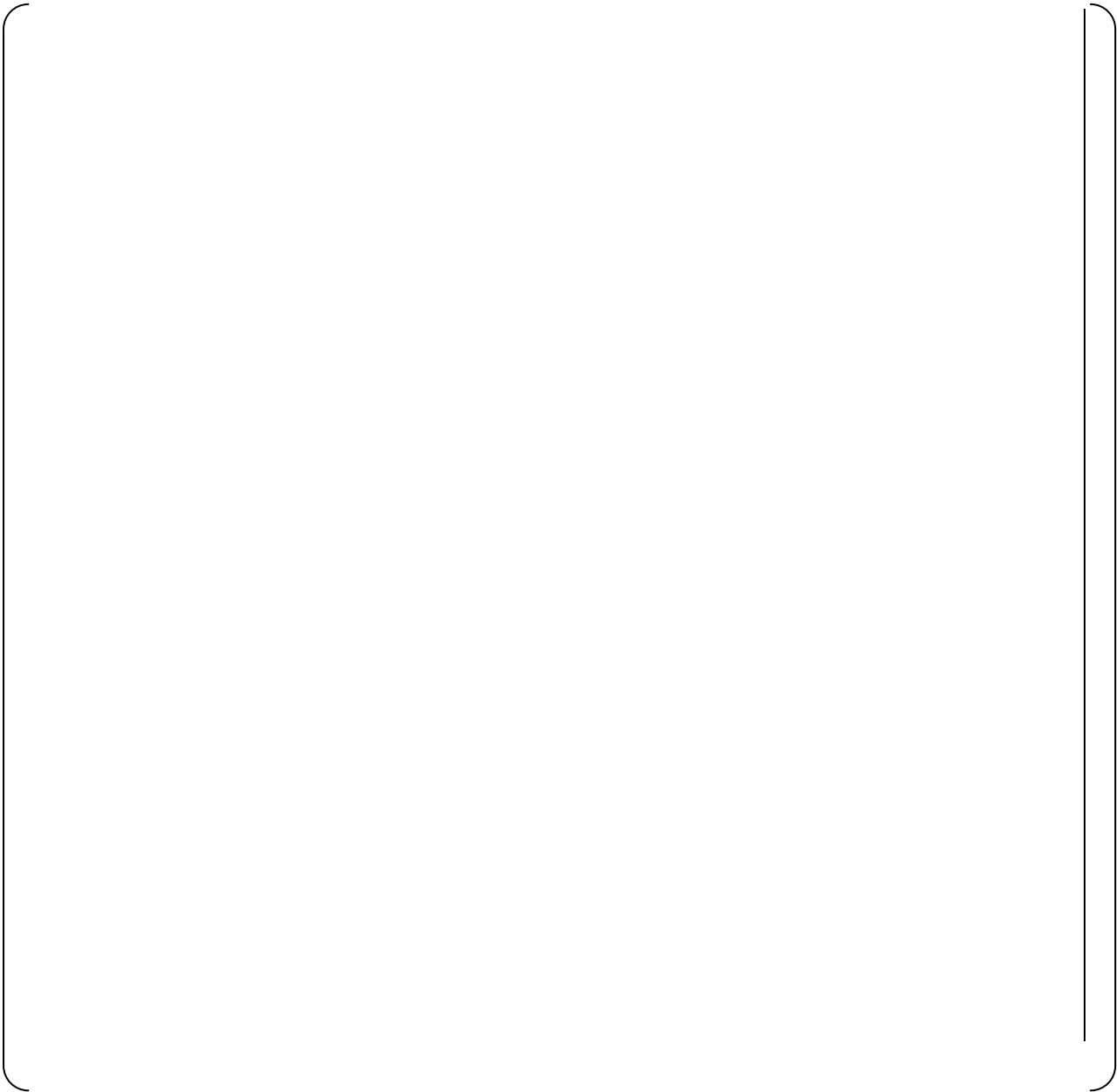
**Figure I-2 Velocity Distributions and Cavitation Pressure Margin at Throat**



**Figure I-3 Relative Average Total Pressure of Forward Flow Area**

**Table I-2 Calculation Results (1/2 Scale)**

**Table I-3 Calculation Results (1/1 Scale)**



## Appendix- J

### Details of Comparison Error for Large Flow

Figure J-1 shows comparison error between test data and CFD results for large flow. Almost all CFD results are within the range of instrument uncertainty of test data. Therefore, model tuning is not necessary for the large flow evaluation.

In Figure J-1, one point in seven points is beyond the  $2\sigma$  limits of the test result. The probability that one point in seven points is beyond the limits of  $2\sigma$  of test result can be calculated by the following expressions.

The probability that the CFD result is within the limits of  $2\sigma$  of test result : [            ]

The probability that the CFD result is beyond the limits of  $2\sigma$  of test result : [            ]

The probability that one point in seven points is beyond the limits of  $2\sigma$  of test results  
[                      ]  
[            ]

The probability that one point in seven points is beyond the limits of  $2\sigma$  is about [      ].  
The conclusion is that, due to the limited number of sample points, this outlier is determined not to be statically significant.



**Figure J-1 Overlapping between Test Results and  
Calculation Results for Flow Rate Coefficient  
(Large Flow Condition)**